Delft University of Technology

Master Thesis

Non-linear Time History modelling of damage initiation and development in an Unreinforced Masonry cavity wall under out-of-plane loading

A thesis submitted to the Delft University of Technology in partial fulfillment
of the requirements for the degree of

Master of Science in Civil Engineering

by

Amey Joshi

February 2023

Amey Joshi: *Non-linear Time History modelling of damage initiation and development in an Unreinforced Masonry cavity wall under out-of-plane loading* (2023)
The electronic version of this thesis is available on:
http://repository.tudelft.nl.

The work in this thesis was done in collaboration with Delft university of technology and TNO:

Applied Mechanics
Department of Structural Engineering
Faculty of Civil Engineering & Geosciences
Delft University of Technology

Structural Dynamics
Building, Infrastructure and Maritime

University Supervisors:	Prof. Dr. ir. Max Hendriks
	Dr. Anjali Mehrotra
	Ir. Paul Korswagen
TNO Supervisors:	Ir. Okke Bronkhorst
	Ir. Jelme Pennings

ABSTRACT

The light and frequent earthquakes in the north of the Netherlands, particularly in the province of Groningen, have recently exposed the unreinforced masonry structures to seismic activities. Since these structures do not adhere to seismic regulations, they are considered vulnerable to seismicity. The ultimate state capacity of the structures is important for an individual's safety, however, these earthquakes are of low intensity and cause aesthetic damage.

In order to investigate the light damage initiation and development, TNO has performed shaking table tests on an unreinforced masonry (URM) cavity wall specimen in out-of-plane (OOP) one-way bending with small increments in intensity. The test specimen consisted of calcium silicate brick inner leaf and perforated clay brick outer leaf. The damage development in the outer leaf was monitored during these tests using a high-speed digital image correlation (DIC) technique to study the initiation and development of damage in the outer leaf of the specimen. The experimental tests showed damage initiation at the mid-height of the outer leaf. The tests could not capture the development of cracks through the thickness of the cavity wall.

The scope of this research is a numerical assessment of the experimental study by using a Non-Linear Time History (NLTH) analysis of light damage initiation and development of a URM cavity wall under out-of-plane loading. The high-resolution experimental results are used as a basis for the development and calibration of models which can better predict the crack initiation and development in URM. The finite element software DIANA 10.5 FEA was used to set up the numerical model and conduct transient analysis.

The seismic signal as an input loading and the top boundary condition of the test specimen. The acceleration data measured from the shaking table tests at the base was used as an input seismic signal for the transient analysis of the models. The input signal needed to be processed before application as the presence of low-frequency content leaded to inaccurate results. Different approaches are discussed in this thesis regarding the processing of the input acceleration signal.

The experimental tests were modeled along the cross-section of the test specimen, thereby highlighting the thickness of the inner leaf and the outer leaf. This enabled tracking the light damage initiation and propagation through the thickness of the cavity wall. A total of thirteen shaking table tests were conducted on the experimental setup. In order to gain insight into the behavior of the specimen during each shaking table test, a model was created corresponding to each shak-

ing table test. Preliminary analysis schemes were set in order to check the validity of all thirteen models. The two cases of top boundary conditions were checked, roller support and spring-mass support. The roller boundary condition proved to be stiff in comparison to the experimental results.

The numerical results were calibrated on the basis of material properties. The results were compared to experimental results by checking the dynamic behavior at the mid-height, dynamic behavior over the height, and light damage initiation and development of the specimen. The results of the numerical models were stiff in comparison to the experimental results. According to the conclusions, it is recommended to research further regarding the boundary conditions, especially the bottom boundary condition due to the formation of a rocking crack. Another important aspect to focus on is the combination of all input signal, thereby, taking into consideration the damage accumulation.

ACKNOWLEDGEMENTS

I want to start by thanking TU Delft and TNO for allowing me to research this topic. I am grateful that I could make a small contribution to the field of civil engineering. This topic was quite interesting and complex with many challenges along the way. My sincere thanks to my company supervisors ir. Okke Bronkhorst and ir. Jelme Pennings who helped me develop a mindset of a researcher. I thank my university supervisors Dr. Anjali Mehrotra, Prof. Max Hendriks, and ir. Paul Korswagen for guiding me through my thesis.

Furthermore, I express my gratitude to ir. Davide Moretti and ir. Thomas van Dijk from TNO for their support and patience in willingly answering my questions. Special thanks to ir. Manimaran Pari and ir. Michele Longo for providing support with the numerical modeling.

I am quite fortunate to have so many friends who supported me during my thesis, and I am grateful. I would like to thank my friends Firas Alshare, Sofia Papoulidou, Stephanie Ramos, and Antonis Tzioumakas for supporting me since the beginning of my master's. They supported and motivated me throughout my entire journey at TU Delft. Most importantly I would like to thank my Mom and my family, they gave me the support and the courage to keep moving forward. This journey would not have been possible without them.

CONTENTS

1 INTRODUCTION

1.1 BACKGROUND

The Netherlands is a country without much natural seismic activity. In the past few decades, a number of small-magnitude seismic occurrences have been brought on by the 1960s-era gas reservoir exploitation. These seismic occurrences are linked to the Groningen region, which contains the largest gas field in the area.

The majority of the area's structures are unreinforced masonry. Terrace homes, semi-detached homes, detached homes, cottages, mansions, and villas are just a few of the various types of residential structures that are present in this region. The majority of structures are terraced houses, which are two-story units connected in a succession to form a building block. Due to the fact that these structures don't adhere to any seismic regulations, they are considered vulnerable to seismicity Figure 1.1.

These constructions have peculiarities that are related to the existence of cavity walls, the quality of the material, which affects the capacity, and the design, which includes supporting walls only in one direction. The structural response of URM under such conditions is often characterized by the development of cracks in the masonry leading to partial and/or complete collapse.

Figure 1.1: Damage to unreinforced masonry structures due to earthquakes.

Most of the research effort so far has been related to safety. However, the observed vibration levels in Groningen are more likely to induce aesthetic damage than severe structural damage. Aesthetic or light damage is particularly difficult to assess as it is invisible to the naked eye as damage initiates in the form of invisible hairline cracks.

In addition to safety, it is crucial to predict and assess the 'light' damage caused by these induced ground motions because it is connected to societal unrest, serviceability losses, and financial losses.

Korswagen et al.[14] performed a combined experimental and Nonlinear Time History (NLTH) study on light damage initiation and development in a URM wall under in-plane cyclic loading. This study showed that the high-resolution data provides a good basis for the development and calibration of models which can better predict the crack initiation and development in URM. Such modeling approaches are needed to provide a reliable assessment of visual damage.

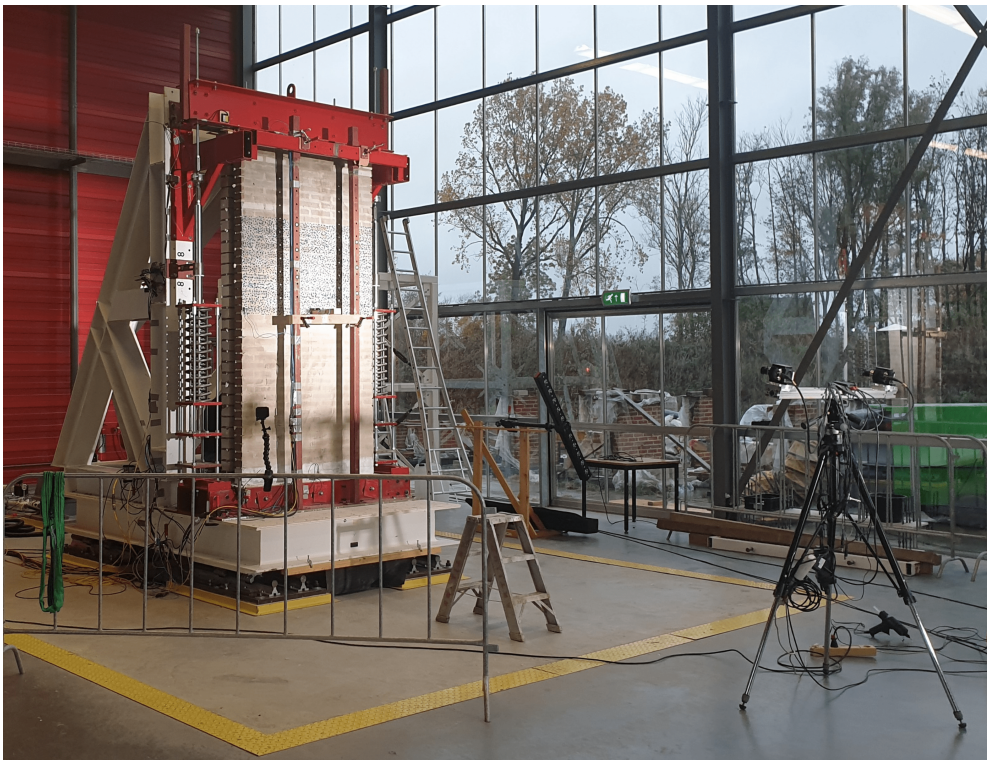

Figure 1.2: Experimental Setup

TNO has performed shaking table tests Figure 1.2 on a URM cavity wall specimen in out-of-plane one-way bending with small increments in intensity. The damage development in the outer leaf was monitored during these tests using a high-speed digital image correlation (DIC) technique to study the initiation and development of damage in the outer leaf of the specimen. The DIC results show that cracks initiated in the specimen during a seismic test were not visible in the visual damage inspection after the test. Only in tests performed at higher intensity visual damage was observed in the outer leaf.

This study aims to develop a numerical model with which the initiation and development of damage in a cavity wall specimen under out-of-plane loading are simulated and compared with the experimental results. After a comparison of the results, The input parameters of

the model are calibrated based on the model's response compared to the experimental response.

1.2 RESEARCH QUESTIONS

In order to develop a numerical model that provides a reliable assessment of the shaking table tests conducted by TNO, the main research question is framed as follows:

"How to numerically assess the development of light damage in URM cavity wall under out-of-plane shaking?"

To answer the main research question, the following sub-questions are formulated as follows:

1. *How to replicate the experimental setup as a numerical model?*
2. *How to calibrate the dynamic behavior of the numerical model?*
3. *How to compare the damage development of the numerical model?*

The goal is to investigate the phenomena of crack initiation and propagation in masonry for recently, generated earthquakes with a thorough examination of crack patterns, crack widths, and the impact of repetitive and combined loadings. The development of numerical models will allow for the analysis of damage progression in more complicated circumstances, such as those including the combined effects of seismicity and diverse settlements or varied thermal motions.

1.3 APPROACH

A research methodology had to be created in order to address the research questions indicated above. An initial numerical model is created using finite element modeling. To begin answering the main research question, it is important to set up a finite element model that provides reliable results. The reliability of results provided by the finite element model with respect to experimental tests was based on a comparison of the following results:

- Material properties of the test specimen.
- Dynamic behavior at the mid-height of the test specimen.
- Dynamic behavior over the height of the test specimen.

- Light damage initiation and development

The model's various parameters can be calibrated based on the experimental results by numerically simulating this test. The report goes into greater depth about the choices made during the process. The numerical models and analyses executed are carried out in finite element software DIANA FEA 10.5. It is capable of taking into account the transient effect of dynamic loading. DIANA FEA 10.5 offers an Engineering Masonry material model for the simulation of the nonlinear behavior of the URM cavity wall.

1.4 THESIS OUTLINE

This thesis consists of 8 chapters. Chapter 1 provides an introduction to this research along with the motivation research questions and methodology. Chapter 2 the theory and literature review on the behavior and modeling of Unreinforced masonry structures (URM) is presented. Chapter 3 presents the important characteristics and results of shaking table tests conducted by TNO(2020). In Chapter 4, the processing of experimental test output is presented. Following this, Chapter 5 describes the setup process of numerical models. Chapter 6 presents the methods of analysis used to evaluate the output of FEM so they can be compared to the results of experimental tests. In Chapter 7, the results of numerical models are compared to the experimental results. Finally, in Chapter 8 conclusions are made and recommendations for further research are suggested.

2 LITERATURE REVIEW

The goal of this literature review is to provide insight into the seismic behavior of unreinforced masonry structures and the procedures for evaluating them. Understanding the properties of the material and analyzing the failure mechanisms are seen as being crucial first steps. Based on the characteristics of the experimental setup, the main method to analyze the seismic behavior is discussed. The non-linear method in focus is the non-linear time history analysis. Following the literature review of the damage states presented.

2.1 MATERIAL DESCRIPTION OF URM

Depending on the construction type used, masonry can be divided into three primary categories. These consist of:

- Unreinforced masonry (URM), which is a term for independent masonry components and has historically been used to build masonry constructions.
- Reinforced masonry in which the masonry is reinforced using steel bars.
- Confined masonry is made up of masonry walls and RC members that are built on all sides, both horizontally and vertically.

The focus of this research is unreinforced masonry (URM). The interaction between mortar and brick units defines the material's behavior in unreinforced masonry. The vertical joints between the bricks are called the head joints and the horizontal joints are called the bed joints. Since bed joints form a continuous connection over the width of a wall and head joints are interrupted by bricks, the effective properties over a cross-section in the total wall in the vertical direction are different from the horizontal direction[4]. The relevant properties pertaining to this research are tensile strength and fracture energy.

2.1.1 Material properties of individual units

To accurately simulate the behavior of the masonry in numerical calculations, certain parameters are required. The masonry is made up

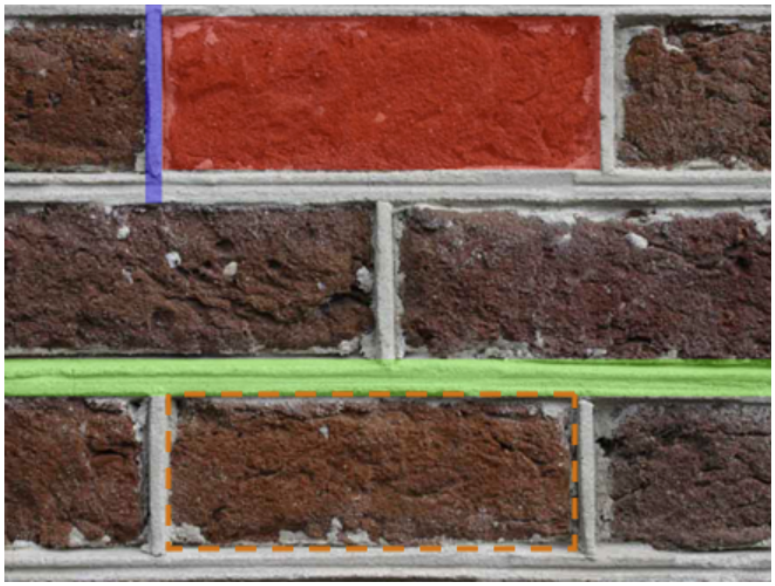

Figure 2.1: Sample of a masonry wall. The colors red, green and blue represent bricks, bed joints and head joint respectively.

of individual units, brick units, and mortar units. In this section, the mechanical properties of the individual units are presented. The orthotropic behavior of the material and the fact that it is made of two separate materials, each with a wide range of material property values, highlights the variability of material parameters.

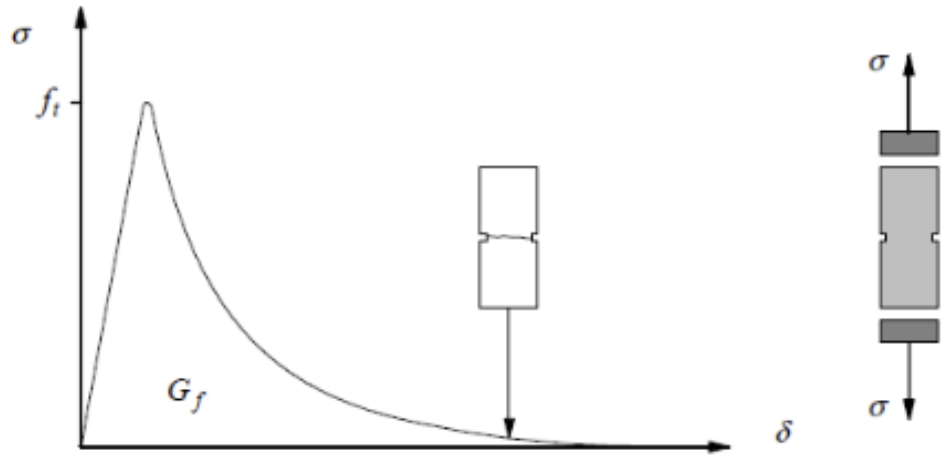

Figure 2.2: Tensile behavior of stone like materials after [20].

Starting with a linear elastic component, tensile behavior continues until the tensile strength is reached and the first fracture appears Figure 2.2. After that, softening occurs, which is shown by a decrease in the material's stiffness as well as a reduction in the load applied to the material sample.

The total fracture energy can be determined from the diagram in Figure 2.2 by integrating the stress-displacement curve. When both stiffness and strength are zero, the material is regarded as entirely failing. Van der Pluijm (1992) [20] conducted some studies on the tensile behavior of bricks and discovered tensile strengths between 1.5 N/mm2 and 3.5 N/mm2 as well as fracture energies between 0.06 N/mm and 0.13 N/mm.

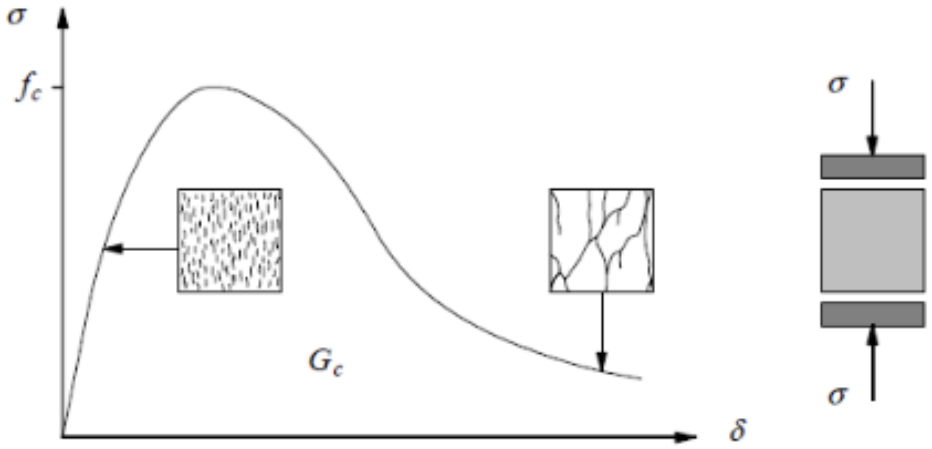

Figure 2.3: Compression behavior of stone like materials after [20].

Compressive behavior Figure 2.3 also begins with an elastic linear portion up until the onset of the first microcracks. At that point, the hardening process begins, which implies that the material's stiffness starts to decline but the load can still grow. This process continues until a large number of small microcracks come together to form a larger macrocrack. After that, the stress-softening strain diagram's phase begins, during which the size and number of cracks grow.

In spite of the number of cracks that have formed, the ultimate stage is a plateau since in compression some strength is still there. It is difficult to establish a reliable assumption about the fracture energy because there aren't enough well-researched experiments on the uniaxial post peak behavior of bricks and mortar under compression.

2.1.2 Mechanical properties of brick-mortar interface

The weakest points of the masonry structure are along the brick-mortar interfaces. Cracks are observed at these locations. The strength of the interfaces depends on ratio of water used in mortar and distribution of mortar on the surface of the brick. Bricks and mortar themselves can have high strength, but due to the interface strength, the overall strength of the masonry is significantly affected. Experimental studies by Van der Pluijm (1992) [20] show that the connection between the bricks and mortar is not consistently spread throughout the complete contact surface area. Figure 2.4 highlights the net bond surface area between the bricks and the mortar.

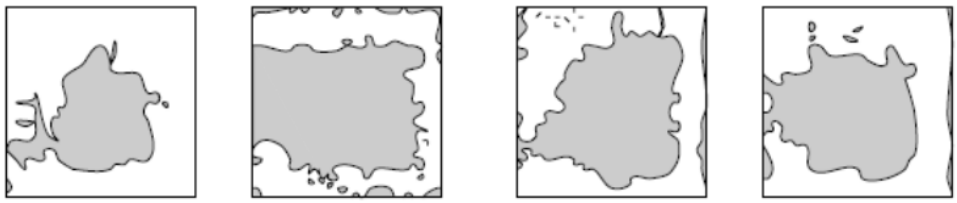

Figure 2.4: Net bond surface area after Van der Pluijm (1992) [20].

Corresponding to mode 1 failure in Figure 2.5a, the tensile behavior of the interface shows exponential softening in Figure 2.6a. Tensile bond strengths between 0.3 and 0.9 $N/mm2$ and mode I fracture energies ($G_{ft}{}^{I}$) between 0.005 and 0.03 N/mm have been discovered.

(a) Mode 1 failure **(b)** Mode 2 failure

Figure 2.5: Modes of failure of tensile and shear behaviour respectively after Van der Pluijm (1992) [20]

Similarly, an exponential softening is observed for shear behavior Figure 2.5b and Figure 2.6b. The shear behavior was evaluated by the application of compression in the normal direction. However, when the sample is also loaded in compression in the normal direction, the residual cohesiveness of the interface does not approach zero. Cohesion values between 0.1 and 1.8 N/mm^2 and mode II fracture energies ($G_{ft}{}^{I}I$) between 0.01 and 0.25 N/mm are found.

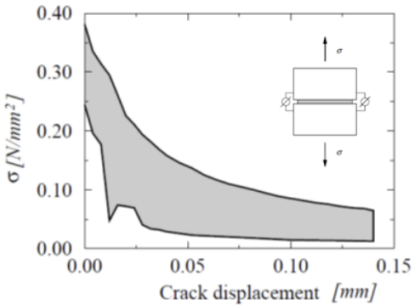

(a) Tensile behavior of interfaces.

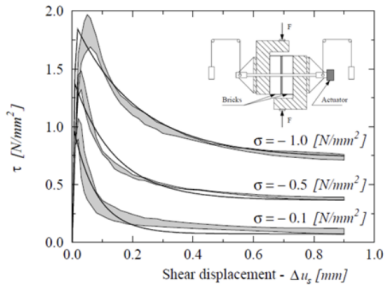

(b) Shear behavior of interfaces.

Figure 2.6: Behavior of interfaces for unreinforced masory after Van der Pluijm (1992) [20]

2.1.3 Material properties of masonry

Often, it is assumed that the characteristics of the components of masonry composites are isotropic. However, because of the geometrical placement of the units and mortar, the brickwork exhibits anisotropy in its effective constitutive behavior [16]. The composite material's behavior is influenced by the qualities of its constituents, its organization, the characteristics of its interfaces, and the loading direction. The behavior of masonry is frequently characterized as orthotropic, which indicates that the material properties in any arbitrary direction may be understood based on those in mutually perpendicular directions [16].

2.1.4 Cavity walls

In the northern part of the Netherlands, in the province of Groningen, the majority of unreinforced masonry walls are cavity walls. A cavity is left between the two leaves of bricks when building a wall in the cavity construction method. Occasionally, insulating material is placed into the cavity. The internal leaf of a cavity wall is a load-bearing wall that carries the vertical loads transmitted by the floors and roof, while the external leaf is frequently a brick veneer wall with no load-bearing function [19].

The inner leaf frequently contains different elements than the outer leaf. The usage of clay bricks for the outside wall and calcium silicate bricks for the inner wall. It is common practice to use metal cavity ties, which can vary in material, form, and spacing, to join the leaves on either side of a cavity wall. Due to the material mismatch, the URM wall's section is assumed to be asymmetric, and as a result, the reaction is direction dependent. Thus, the direction that the ground motion is acting is crucial in terms of earthquake loading[21].

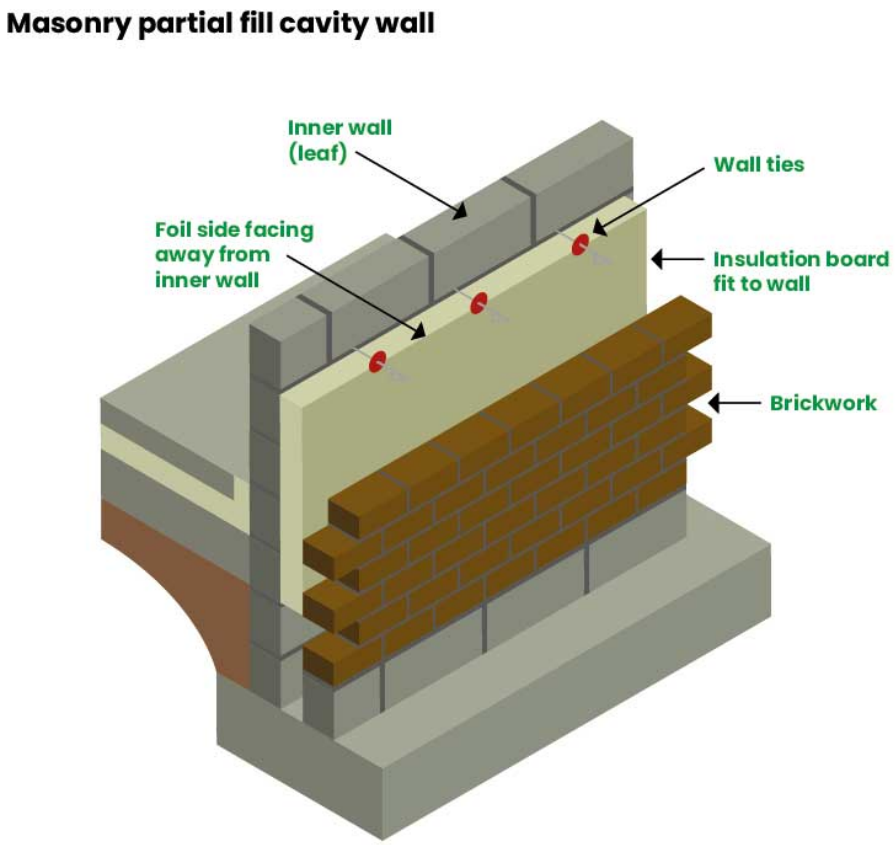

Figure 2.7: Example of an unreinforced masonry cavity wall.

2.2 OUT-OF-PLANE BEHAVIOR OF URM WALLS

Recently, human-induced seismicity exposed some of these previously earthquake-free zones to seismic activity, highlighting the shortcomings of existing construction methods and the absence of seismic details [21]. The out-of-plane behavior of load-bearing walls, according to research by [3; 19; 21; 17], is the primary factor in the destruction and failure of masonry structures when subjected to seismic loads.

Figure 2.8: Examples of out-of-plane damage to masonry buildings

Figure 2.8 presents examples of the failure of masonry structures due to out-of-plane behavior. This out-of-plane behavior is mostly

influenced by the walls' support circumstances. Different crack patterns can be seen as the wall is loaded out-of-plane depending on the support conditions [22].

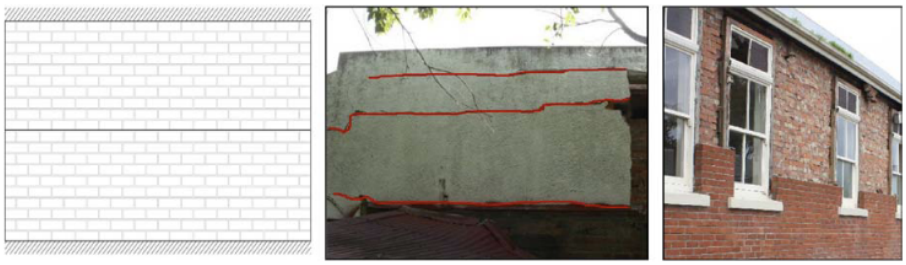

(a) Schematic example of one-way bending type failure

(b) Horizontal cracking (highlighted in red for clarity)

(c) Collapse of the outer leaf

Figure 2.9: Out-of-plane one-way bending type failure. (a) Schematic example of one-way bending type failure.(b) Horizontal cracking (highlighted in red for clarity). (c) The collapse of the outer leaf [5].

Walls with no support on either side develop a cracking pattern known as unidirectional bending failure Figure 2.9. The wall experiences a vertical axial load, which causes it to crack at its supports and midpoint, with the wall's two parts behaving as rigid bodies.

For walls that are supported at all sides, a bidirectional bending failure pattern is observed Figure 2.10. Two-way out-of-plane bending type failure is frequently encountered in URM walls that are subjected to earthquake-induced shaking. Due to a combination of factors including boundary conditions and weak mortar strength, a typical U-shaped failure plane typically forms in the top portion of the wall [5].

(a) Schematic example of two-way bending type failure, short span wall (U-shaped)

(b) Typical two-way cracking pattern (highlighted in red for clarity)

(c) Short span cavity-wall with unrestrained top boundary support

Figure 2.10: Out-of-plane two-way bending type failure. (a) Schematic example of two-way bending type failure, short span wall (U-shaped).(b) Typical two-way cracking pattern(highlighted in red for clarity). (c) Short span cavity-wall with unrestrained top boundary support [5].

Shear and sliding failure on mortar joints or between storeys are the two main types of out-of-plane failure. In general, it is thought that

structures with cavity walls are more susceptible to seismic loading than those with solid walls and require careful consideration.*(ARUP, 2013)*

2.3 DAMAGE STATES OF URM

2.3.1 Classification of damage states

According to the European Macroseismic Scale [12], the varying degrees of damage to URM cavity walls are defined as follows:

- *DS0*– No visible damage, no damage to the masonry cavity walls was observed.
- *DS1*–Aesthetic damage, visible hairline cracks along the mortar joints.
- *DS2* – Slight structural damage, visible and significant in-plane failure.
- *DS3*– Moderate structural damage, out-of-plane failure initialised and visible cracks.
- *DS4*–Severe structural damage, partial out-of-plane collapse of cavity-walls or outer leaf.
- *DS5*–Extreme structural damage, the collapse of masonry cavity walls.

(a) D0 - None Visible (b) D1 - Insignificant (c) D2 - Minor

(d) D3 - Moderate (e) D4 - Severe (f) D5 - Extreme

Figure 2.11: Examples of damage states [10].

This light damage corresponds to Damage State 1 (DS1). The initial damage state or damage grade (DS1) denotes minimal structural damage and minor non-structural damage, which appears as hairline wall cracks and plaster damage.

2.3.2 Quantification of aesthetic or light damage

The focus of this research is light damage initiation and propagation. Korswagen [13] proposed a damage scale and parameter that objectively quantifies light damage due to cracking in masonry walls. The parameter assesses the progression and accumulation of damage by using cracking as an expression for light damage in masonry walls.

A dimensionless damage level parameter (Ψ_D or Ψ) Equation 2.1 was proposed by [13].

$$\Psi = 2 * n_c^{0.15} * \hat{c}_w^{0.3} \tag{2.1}$$

Here, the number of cracks in the wall or specimen is represented by n_c, and $\hat{c}_w$ is the width-weighted and length-averaged crack width (in mm) that was determined using Equation 2.2. c_w is the maximum crack width along each crack in mm; c_L is the crack length in mm.

$$\hat{c}_w = \frac{\sum_{i-1}^{nc} c_{w,i}^2 * c_{L,i}}{\sum_{i-1}^{nc} c_{w,i} * c_{L,i}} \tag{2.2}$$

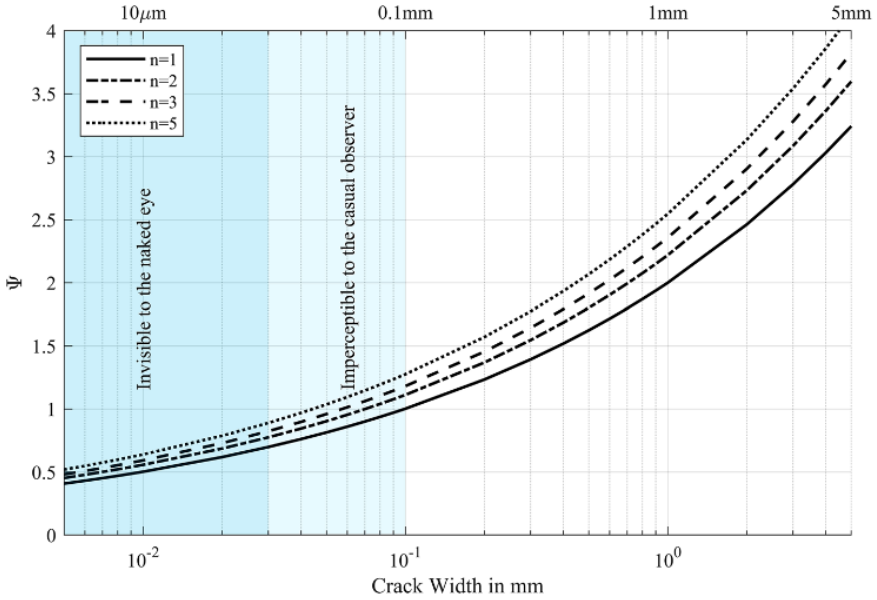

Figure 2.12: The relationship between Ψ for a specified crack-width is shown. For multiple cracks (n ¿ 1) it is assumed that all cracks are of the same width.Taken from [13].

Regardless of the specimen size, the parameter enables comparison of the degree of damage Ψ. This is consistent with the parent damage scale (DS1-DS5), where only the significance of the damage to each particular structure is taken into account and the damage states are independent of the size of the structure. This is especially useful for tracking the development of damage and comparing it between samples of various diameters.

Additionally, because the parameter (Ψ) relates to how easily the damage can be repaired when the area of the damaged wall is multiplied by the parameter, the cost of the repair may be determined directly.

Damage state	DS0	DS1			DS2
Damage level	DL0	DL1	DL2	DL3	DL4
Parameter of damage	$\Psi_D < 1$	$1 < \Psi_D < 1.4$	$1.5 < \Psi_D < 2.4$	$2.5 < \Psi_D < 3.4$	$\Psi_D > 3.5$
Aproximate crack width	Imperceptible cracks	Up to 0.1 mm	Up to 1 mm	Up to 5 mm	5–15 mm

Figure 2.13: The damage parameter is discretized on the basis of damage sub-levels. Taken from [13].

The Damage State 1 (DS1) is divided into further sub-scales on the basis of ease of repair. The hairline cracks belong to the first level(DL1) with approximated crack width up to 0.1 *mm*. Fine cracks that are simple to cure during standard decorating. Possibly a single, minor crack in the building. Exterior brickwork has noticeable cracks, found at careful inspection belonging to the second level (DL2). Cracks with widths up to 1 *mm* belong to this level.

Cracks are evident from the outside, and repainting may be necessary to ensure water tightness with approximate width up to 5 *mm* belongs to the third level (DL3). The parameter expresses the total number of visible cracks as a single number such that the smallest visible cracks, with a width of 0.1 mm, corresponding to a value of about one (Ψ = 1), slightly larger cracks, with a width of close to 1 mm, to two (Ψ = 2), and cracks, with a width of roughly 4 mm, to three (Ψ = 3). This range is defined in Figure 2.13.

2.4 COMPUTATIONAL MODELING OF MASONRY STRUCTURES

2.4.1 Modelling strategies

The scientific community has consistently worked on the computational analysis of masonry structures during the past 50 years. The need for non-linear evaluation techniques is highlighted by the prevalence of cracking in URM buildings at low seismic demand levels. This kind of building frequently lacks the strength to withstand lateral seismic loads, and it is particularly unable to disperse energy and take advantage of ductility. The modeling of masonry structures is suggested using several methods.

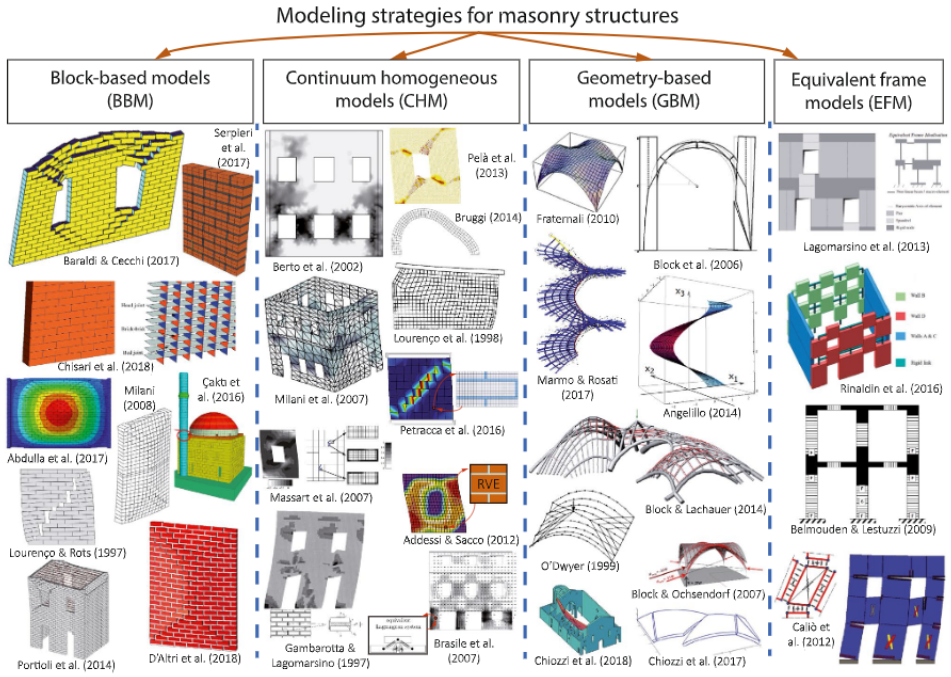

Figure 2.14: Existing techniques for modelling URM[7].

The main variations relate to the scope of research and the terminology used to describe masonry. The primary modeling techniques can be divided into the following categories [7]:

1. Block-based models (BBM)
2. Continuum models (CM)
3. Macroelement models (MM)
4. Geometry-based models (GBM)

Masonry is a composite material with anisotropic behavior. This is related to the precise positioning of the units and mortar joints. Pertaining to the focus of this study, the continuum modeling strategy is

chosen due to its simplicity. Within the continuum modeling strategy, three approaches can be taken to model masonry. The three approaches are categorized on the basis of accuracy and simplicity desired [16]:

- Detailed micro-modeling
- Simplified micro-modeling
- Macro-modeling

In this strategy, masonry can be numerically represented by modeling each sub-element independently using a micro-modeling technique or by using a macro-modeling approach that models the entire structure as a continuum [16]. However, it does not include the representation of the local elastic and inelastic mortar mechanisms, which are thought to be appropriate for the analysis of massive structures. In the simplified micro-modeling approach, the brick units are represented as continuum elements. Discontinuous elements are used to represent the behavior of the mortar and unit-mortar interface. As the mortar has no physical thickness in the approach, to preserve the original dimensions, the dimensions of brick units are expanded.

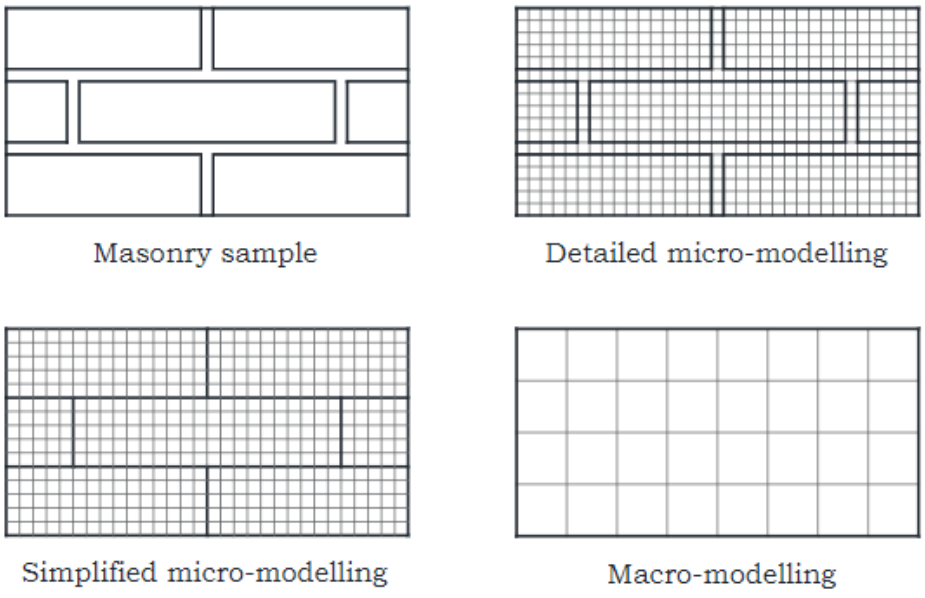

Figure 2.15: Modelling strategies of URM [19].

The macro-modeling method views masonry as a homogeneous material in which there is no differentiation between units and joints. Although masonry is typically periodic in nature, it is acceptable for homogenization procedures to ”smear out” the properties of the units and joints over the sample. A smeared crack approach may be used to capture local cracking and softening of the masonry.

Given the numerous discontinuities in masonry structures, it is debatable whether modeling them as continuum elements can accurately capture their behavior. A continuum model only approximates what occurs at the microscopic level. However, because of increased computational efficiency, there is a lot of interest in creating continuum models for brickwork. Especially for modeling URM cavity walls under out-of-plane loading, the local effects are important. These effects are important considering the strength of the present situation and the accuracy of the model. Therefore, the macro modeling approach is chosen in this study as it can be expanded into a full-scale building model.

2.4.2 Analysis of seismic behavior

An earthquake is a sudden slip on a fault that causes shaking of the ground and the release of seismic energy. Any unexpected stress state in the earth might trigger seismic activity. In the case of Groningen, the earthquakes that are intentionally caused, involve human activity. There are two principal approaches for examining the collapse or near-collapse behavior of masonry structures: (i) incremental-iterative analyses and (ii) limit analysis-based solutions [7]. This study uses the incremental-iterative analysis approach. Analyses that are incrementally iterative can be divided into non-linear static and non-linear dynamic (time history) studies.

Non-linear time history analysis (NLTHA)

The structure is gradually subjected to time-dependent actions in non-linear time history analysis (also known as transient non-linear analysis). The structural response evolves in real-time while also taking damping and inertial effects into consideration.

The consequences of dynamic events (such as earthquakes, impacts, explosions, etc.) on masonry structures can be simulated using Non-linear Time History analysis. The term "non-linear" describes a structural model with non-linear geometrical non-linearities, non-linear constitutive properties, or contact non-linearities. The non-linear analysis in seismic analysis enables designers to closely monitor the structure's reaction to seismic loading until the ultimate or collapse limit states.

In fact, the ability to account for time-dependent stresses enables the simulation of the structure's response to a real accelerogram. Analysis of shaking table experimental testing on masonry constructions is also possible. The outcome of the Non-linear Time History analysis will be a wealth of information, which will include the full response of displacements, stresses, or strains through time for every point on the

structure of interest. Its comprehensive reaction, especially in seismic analysis, is a clear benefit of non-linear dynamic time-history analysis over non-linear pushover analysis, another crucial form of seismic analysis.

Governing equation of motion

The equation of motion (EOM)of a system can be defined as Equation 2.3.

$$\mathbf{M\ddot{U}} + \mathbf{C\dot{U}} + \mathbf{KU} = \mathbf{R} \tag{2.3}$$

Here, the mass, stiffness, and damping matrices are represented by **M**, **C**, and **K**. The $\ddot{\mathbf{U}}$, $\dot{\mathbf{U}}$ and **U** represent the acceleration, velocity, and acceleration vectors. The external forces as a function of time **t** are represented by **R**. For non-linear systems, the generalized derivation of the governing equations can be found in [9]. This derivation takes extra terms into consideration, non-linear damping operator **C**(**u**, $\dot{\mathbf{u}}$) and non-linear operators **S**(**u**). The physical non-linearity of the system can be included in the Equation 2.3 by considering time variation in stiffness **K** and damping **C** matrices.

Time integration methods

To approximately satisfy the equations of motion throughout each time step of the analysis, time integration techniques are used. For Non-linear Time History analysis, the only practical solution procedures direct time integration. Direct time integration is the process of directly integrating the system's equations of motion (EOMs) shown in Equation 2.3 in the time domain without first transforming them into another form.

The system's governing equations must first be derived before using the direct time integration methods. It is convenient to start with the equilibrium equations governing the linear system because, in theory, they share the same fundamental idea and methodologies for direct time integration for both linear and non-linear systems.

The most popular time integration schemes in structural mechanics are the Newmark integration schemes. The Newmark integration system might be implicit or explicit depending on the parameters chosen, and selecting the right settings could lead to a variety of well-known integrators. Equation 2.4 and Equation 2.5 present the assumptions made in the Newmark scheme [6].

$$\ddot{\mathbf{U}}^{t+\Delta t} = \dot{\mathbf{U}}^{t} + [(1-\gamma)\ddot{\mathbf{U}}^{t} + \gamma\ddot{\mathbf{U}}^{t+\Delta t}]\Delta t \tag{2.4}$$

$$\mathbf{U}^{t+\Delta t} = \mathbf{U}^t \Delta t + \dot{\mathbf{U}}^t + [(1/2 - \beta)\ddot{\mathbf{U}}^t + \beta \ddot{\mathbf{U}}^{t+\Delta t}]\Delta t^2 \tag{2.5}$$

The physical quantities displacement, velocity and acceleration are known at time t. The physical quantities are unknown at time $t + \Delta t$. The properties of the Newmark scheme is determined by the parameters γ and β. The Newmark scheme is considered implicit and unconditionally stable for $2\beta \geq \gamma \geq 1/2$. This method has an accuracy of $O(\Delta t^2)$. This method can be used by evaluating the Equation 2.3 at $t + \Delta t$. The details of the Newmark scheme are described in the book [2].

3 EXPERIMENTAL TESTS ON URM CAVITY WALL BY TNO (2020)

This chapter presents the details of the experimental tests conducted by TNO to investigate the out-of-plane behavior of the URM cavity wall. The results obtained from these tests are shown and discussed. The material tests were conducted by Hanzehogeschool Groningen. The focus of these experimental tests was to investigate the light damage development for unidirectional bending failure. The shaking table tests are conducted in one direction, namely the out-of-plane direction of the URM cavity wall. The results from the shaking table tests are used as a basis for the development of numerical models and calibration of results.

3.1 SETUP OF SHAKING TABLE TEST

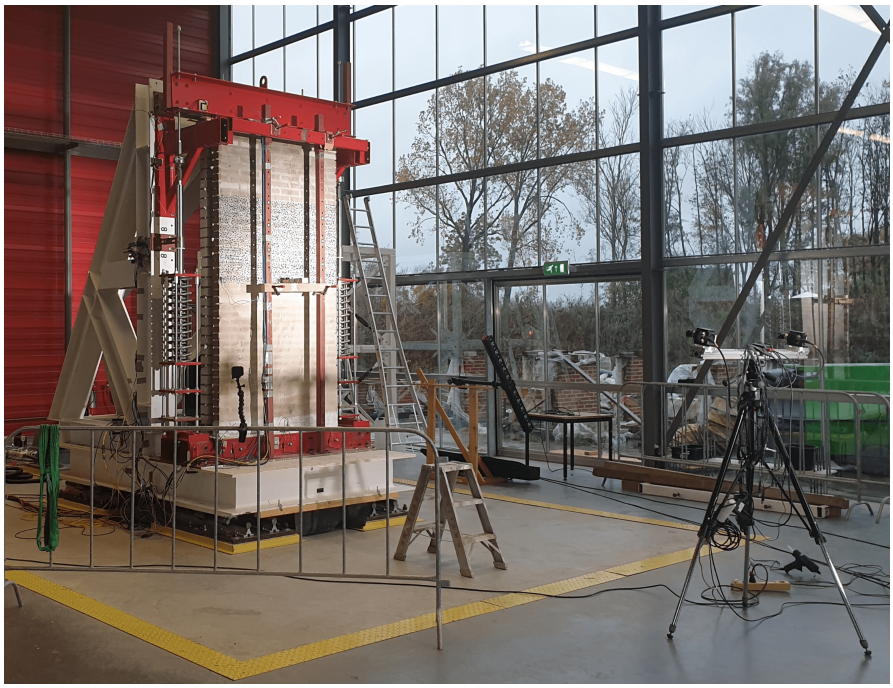

Figure 3.1: Overview of shaking table test setup for URM cavity wall done by TNO(2020)

In Figure 3.1, an overview of the test setup with its components is shown. The tests were performed on the URM cavity wall, which

consists of an inner leaf and an outer leaf. The specimen was placed on a uni-axial shaking table with an approximate surface area of 2 x 3 m^2 and a weight of 3.5 *tonnes*. Figure 3.2 and Figure 3.3 describe the experimental setup. The white support frame was placed at the back of the shaking table. This frame provided support to the red top beam. This beam is connected to the support frame using a hinge condition, allowing translation along the plane of the wall and rotation about its longitudinal axis. The support frame was made as rigid as possible so that the top beam undergoes a similar out-of-plane behavior as applied to the table. This is to ensure that the specimen experiences similar horizontal out-of-plane loading at its top as well as the bottom.

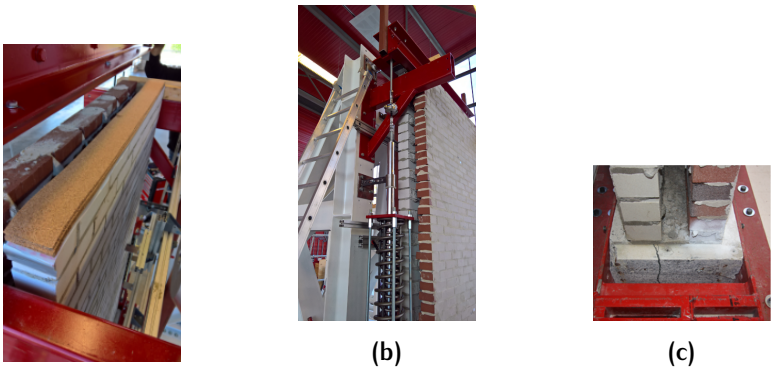

(a) Layers of cork

(b) Prestressing mechanism

(c) Bottom fixed condition

Figure 3.2: Layers of cork between the top beam and inner leaf, prestressing mechanism to create overburden loading and fixed condition for the bottom of the test specimen.

The support conditions and loading conditions of the experimental setup are shown in Figure 3.2. The red beam at the top is used to load the inner leaf of the cavity wall. The weight due to the building components above was simulated as a uniformly distributed load at the top of the inner leaf. Figure 3.2a highlights the layers of cork sheet that are placed between the beam and the upper side of the inner leaf, this ensures uniform distribution of the load.

The prestressing mechanism is shown in Figure 3.2b. The top beam on the top of the inner leaf is prestressed by means of a prestressing spring assembly, thereby applying an overburden load. This prestressing structure pulls on the steel red top beam of the specimen via a tube. The overburden load on the inner leaf is determined by the prestressing force of the springs (F = 9 kN per spring) and the weight of the top beam (300 kg). During the tests on the cavity wall specimen, a load of 18 kN (2 x 9 kN) from the prestressed springs and 3 kN (300 kg) from the top beam was applied as an overburden load. The concrete block on the bottom of the specimen is fixed on the shaking table between two red corner profiles as shown in Figure 3.2c. The

different views of the experimental setup are shown with a schematic setup in Figure 3.3.

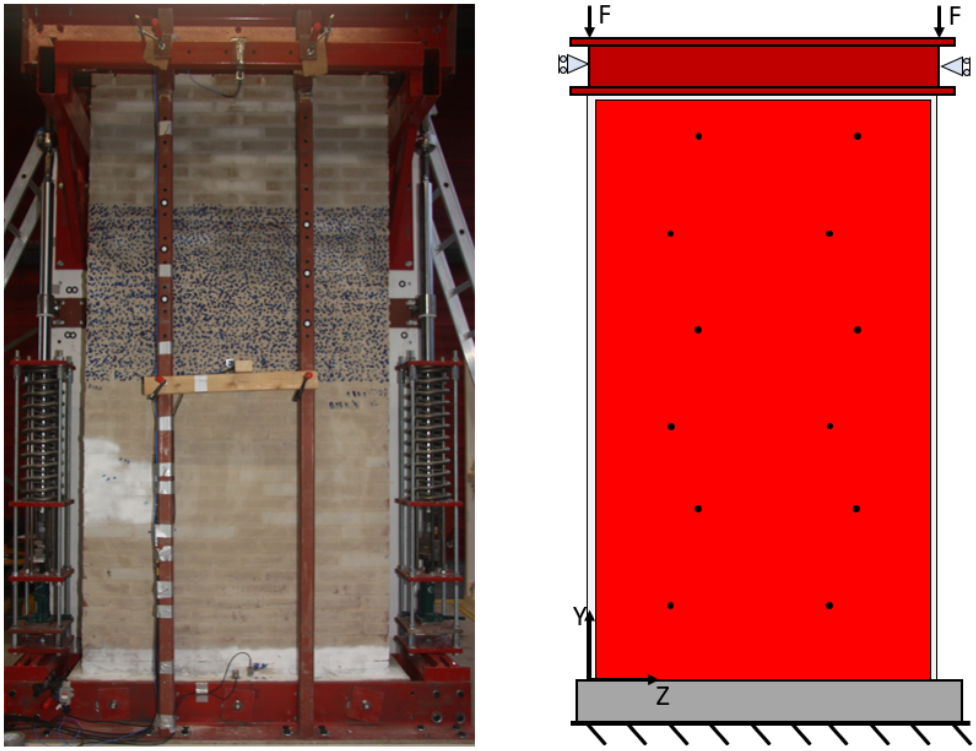

(a) Front view

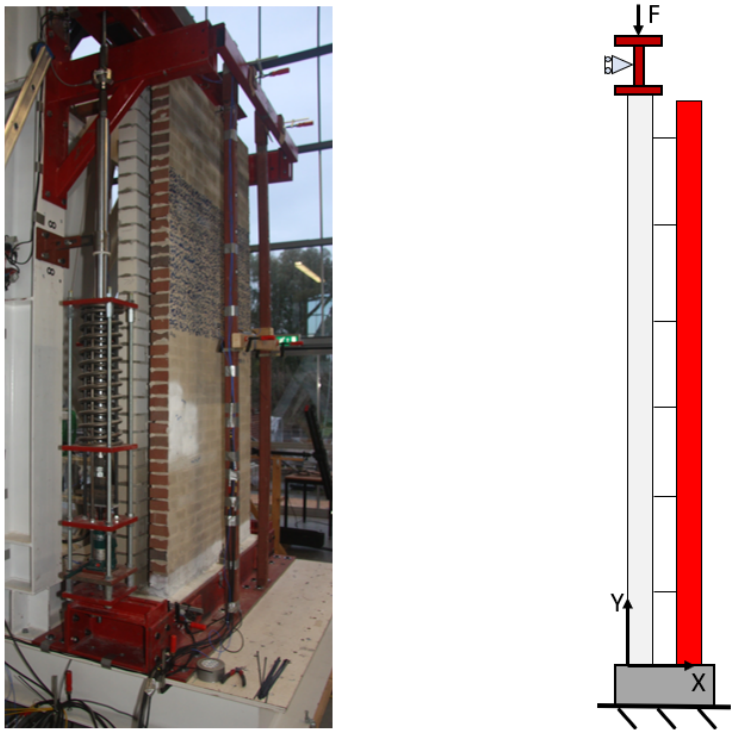

(b) Side view

Figure 3.3: Schematised setup of the experimental shaking table tests.

3.2 TEST SPECIMEN DESCRIPTION

The specimen consisted of an inner and outer leaf. The inner leaf was constructed of white calcium silicate bricks (2.9 kg per brick), Amstel format, manufactured by Calduran Kalkzandsteen BV was used as the inner leaf. The calcium silicate brick was 214 mm wide, 102 mm deep, and 72 mm high. The inner leaf was composed of 32 layers with 6 bricks per layer. The outer leaf of the specimen consisted of Gronings Red perforated bricks (1.6 kg per brick). The perforated bricks are of the type Jupiter, from the company Strating. The dimensions of perforated bricks were 209 mm wide, 99 mm deep, and 50 mm high (waalformaat), stacked in 42 layers, each with 6 bricks per layer. The depth of the cavity between the inner and outer leaf was 80 mm. In this cavity, L-shaped anchors were of Gebroeders Bodegraven UNI-L (32512), with a diameter of 3.6 mm, galvanized thread, and a length of 200 mm. The positions of the anchors are shown in Figure 3.3 and specified in Table 3.1.

Y *[m]*	**Z1** *[m]*	**Z2** *[m]*
0.34	0.28	0.96
0.76	0.41	1.05
1.18	0.29	0.96
1.6	0.41	1.05
2.02	0.3	0.96
2.435	0.39	1.07

Table 3.1: Location of anchors in the specimen, measured from the front view of the shaking table test setup. The coordinate system is defined in Figure 3.3.

3.3 MATERIAL PROPERTIES OF THE TEST SPECIMEN

In order to evaluate the material properties of the specimen shown in Figure 3.3, Hanzehogeschool Groningen conducted tests on the individual units of the specimen. The material properties obtained from the below-mentioned material tests are summarised in Table 3.2.

Unit compression test

Unit compression tests were conducted on the individual brick units of the cavity wall to calculate the compressive strength of the bricks. By using the results of the unit compression tests, the normalized mean compressive strength of the masonry was calculated.

Mortar test

The compressive strength of the mortar used in the inner leaf and outer leaf is calculated using mortar tests. The flexural strength of the mortar was also calculated using mortar tests.

Bond wrench test

The bond wrench test is used to calculate the bond strength between the masonry unit and the mortar. In Figure 3.4, the bond between the brick units and mortar of the inner leaf and outer leaf is shown.

(a) Perforated clay bricks

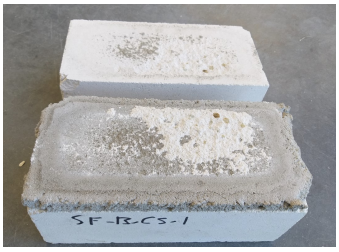

(b) Calcium silicate bricks

Figure 3.4: Bond wrench tests highlighting the bond strength of calcium silicate(inner leaf) and perforated clay bricks(outer leaf).

Out-of-plane bending test

As the focus of the experimental shaking table tests is to investigate the out-of-plane behavior of the cavity wall, out-of-plane bending tests were conducted on small samples of the outer leaf. The out-of-plane bending tests were conducted considering the plane of failure parallel to bed joints Figure 3.5.

Figure 3.5: Out-of-plane bending tests conducted on perforated clay bricks (outer leaf).

Material Properties	Notation	Inner Leaf	Outer Leaf	Unit
Unit compression test				
Compressive strength of unit	f_c	27.6	24.6	N/mm^2
Normalised mean compressive strength	f_b	24	18.5	N/mm^2
Mortar test				
Mean compressive strength of mortar	f_m	7.2	7.2	N/mm^2
Mean bending tensile strength of mortar	f_{mt}	2.4	2.4	N/mm^2
Bond wrench test				
Mean Bond strength minimum	$f_{w,min}$	0.25	0.26	N/mm^2
Mean Bond strength maximum	$f_{w,max}$	0.6	0.59	N/mm^2
Out-of-plane bending test				
Mean flexural strength	f_{xk1}	0.16	0.15	N/mm^2

Table 3.2: Material properties obtained from unit compression tests, mortar tests, and out-of-plane bending tests conducted by Hanzehogeschool Groningen.

3.4 INSTRUMENTATION

Many devices were used to measure the specimen's dynamic behavior. An impact hammer was used to analyze the specimen's dynamic properties, including its inherent frequencies, mode shapes, and damping. By using a Frequency Response Function (FRF) to compare a known input and measured output, it is possible to determine the properties of the system. The force signal of the hammer hit serves as the experiment's known input. The hammer tests were performed before each shaking table test Table 3.4.

To investigate the dynamic behavior of the specimen, sensors were used to capture physical quantities like acceleration and displacements of the specimen at different locations. In Table 3.3, the exact positions of the sensors are shown according to the coordinate system established in Figure 3.6. Acceleration data was collected using acceleration sensors at the concrete block, top beam, and over the height of the specimen.

Displacement data were collected using laser sensors at the mid-height of the specimen. These laser sensors are attached to an aluminum frame. This aluminum frame is attached to the white supporting frame. Similarly, the exact frame is attached at the back of the specimen. In this way, the laser sensors were able to collect displacement data of the specimen at mid-height relative to the shaking table.

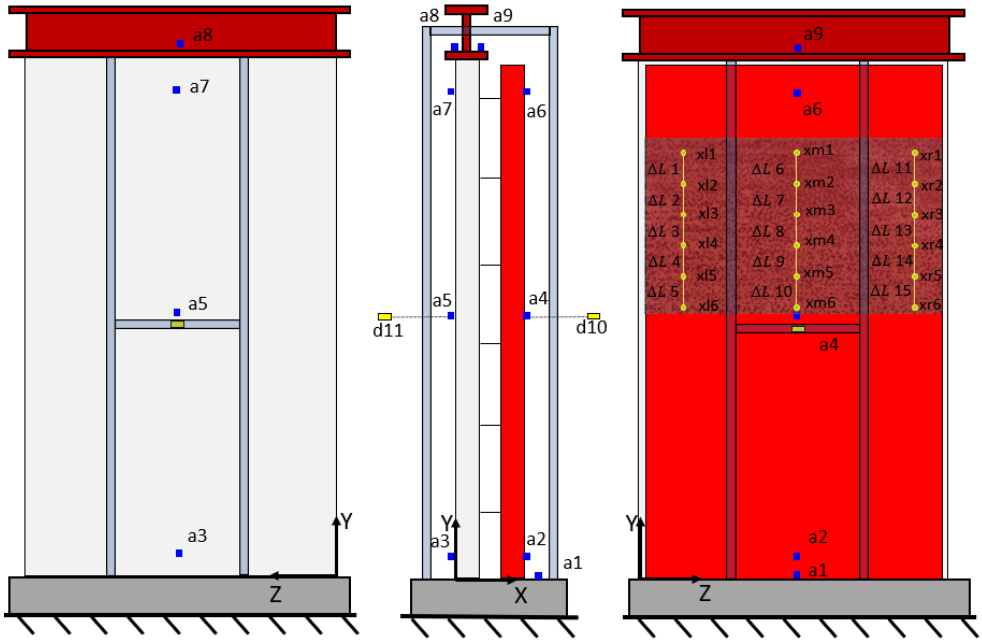

Figure 3.6: Schematic representation of test specimen with acceleration and laser sensors. The laser sensors are placed on the aluminum frame (light grey), which is attached to the supporting white frame.

Sensor locations			
Sensor name	Measurement direction	Positions	
		Y [m]	Z[m]
Inner Leaf			
d11	x	1.305	0.670
a3	x, y	0.004	0.742
a5	x	1.300	0.750
a7	x	2.575	0.705
Outer Leaf			
d10	x	1.310	0.670
a1	x, y, z	0.015	0.665
a2	x, y, z	0.022	0.730
a4	x	1.330	0.634
a6	x	2.593	0.670
Top beam			
a8	y	2.701	0.615
a9	x, y	2.701	0.645

Table 3.3: Locations of acceleration and laser sensors used to collect data. The coordinate system is defined in Figure 3.6.

The propagation of cracks above the mid-height of the outer leaf was tracked using the 2D-Digital Image Correlation (DIC) technique. After the bricklaying of the outer leaf was washed in, a DIC pattern,

consisting of speckles or dots was created on the wall. This pattern helped monitor the out-of-plane displacement of the outer leaf. The same aluminum frame is used to position laser sensors to measure the displacement and crack development of the specimen during the tests.

The yellow circles Figure 3.6, represent the locations where the visual damage inspection was conducted. The damage inspection divided the speckle pattern of the outer leaf into three sections; left (*xl*) middle (*xm*) and right (*xr*). The acceleration sensors are PCB sensors type 3801DFB20G or type 3703G3FD3G. The lasers are SUNX sensors type ANR1150. The data acquisition was performed with a Getac computer type X500, using Dewesoft 7.1.1 software. All sensors were read with a sampling frequency of 500 Hz and filtered with an 8th-order Butterworth low-pass filter.

3.5 SHAKING TABLE TEST INPUT SIGNALS

This research was conducted to get insight into uni-directional bending failure. To simulate this, the specimen was placed on the shaking table, and dynamic input was applied by a hydraulic actuator connected to the table using an input acceleration signal. The input signal (FHUIZ-DS0) Figure 3.7, corresponds to the second floor accelerogram obtained from a TREMURI [15] model of an experimentally tested full-scale house [11] (in an undamaged configuration) when subjected to the ground motion recorded at Huizinge event of April 2012. The input signal was scaled and applied sequentially to the test specimen. The test names and scaling factors of the input signal are described in Table 3.4.

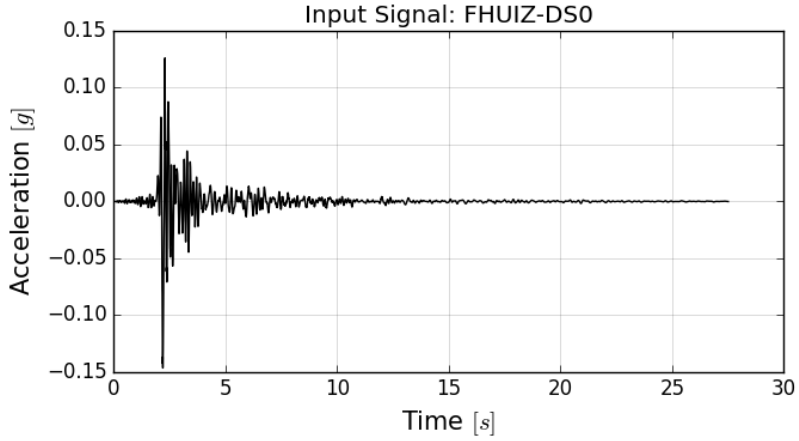

Figure 3.7: Original input signal (FHUIZ-DS0) used for shaking table tests conducted by TNO(2020), obtained from TREMURI[15].

Test Signal name	Scaling factor	PTA [g]	Overburden Load [kN]
FHUIZ-DS0-0002	25%	0.03	18
FHUIZ-DS0-0005	50%	0.07	18
FHUIZ-DS0-0008	75%	0.10	18
FHUIZ-DS0-0011	100%	0.13	18
FHUIZ-DS0-0014	125%	0.16	18
FHUIZ-DS0-0017	150%	0.20	18
FHUIZ-DS0-0020	175%	0.23	18
FHUIZ-DS0-0023	200%	0.26	18
FHUIZ-DS0-0026	220%	0.29	18
FHUIZ-DS0-0029	240%	0.31	18
FHUIZ-DS0-0032	260%	0.34	18
FHUIZ-DS0-0035	270%	0.35	18
FHUIZ-DS0-0038	280%	0.36	18

Table 3.4: Scaling of input signal (FHUIZ-DS0 or FHUIZ-DS0-0011). These thirteen scaled input signals are sequentially applied to the shaking table.

3.6 SHAKING TABLE TEST RESULTS

The results obtained from the shaking table tests conducted by TNO are presented and discussed. In order to analyze the data collected from the sensors, such as acceleration and displacement, preprocessing operations were conducted on the raw data by TNO. The offsets and trends were removed by averaging and filtering the data with a low pass filter. The pass band and stop band frequency of the filter were 48 *Hz* and 52 *Hz* respectively. The measured displacements obtained from the laser sensors were differentiated into velocities and accelerations. The measured accelerations from the acceleration sensors were integrated into velocities and displacements.

3.6.1 Measured data from sensors

Figure 3.8 presents the measured acceleration and displacement signal recorded during the test performed with signal **FHUIZ-DS0-0011** (scaling factor = 100%). The acceleration data was recorded at the concrete block from the acceleration sensor ***a1***. The relative to base displacement signal of the inner leaf and outer leaf is compared in Figure 3.8. As described in Section 3.4, the lasers collected displacement data relative to the shaking table.

The relative to base displacement data were recorded by the laser sensors ***d10*** and ***d11*** at the mid-height of the specimen for the inner and outer leaf respectively. Figure 3.9 presents the data obtained for test with signal **FHUIZ-DS0-0038** (scaling factor = 280%), the signal with the highest peak table acceleration.

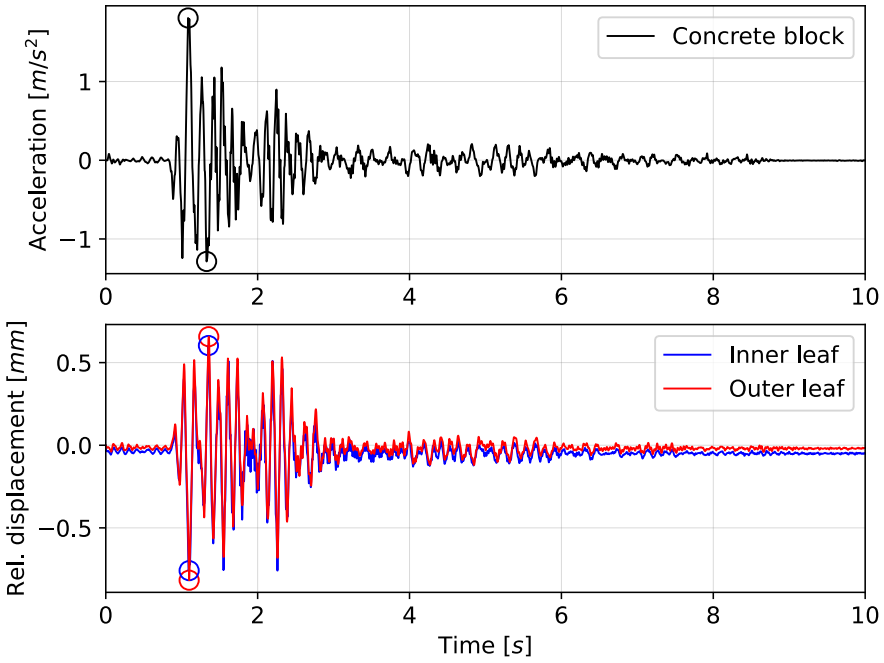

Figure 3.8: Measured data at concrete block (a1), inner leaf (d11) and outer leaf (d10) during the test with input signal FHUIZ-DS0-0011 (scaling factor = 100%).

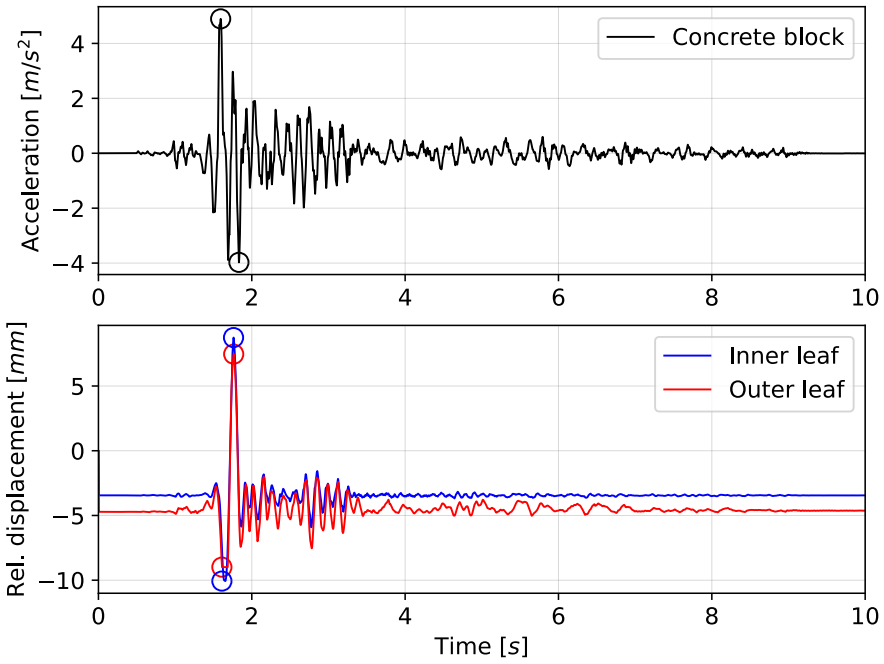

Figure 3.9: Measured data at concrete block (a1), inner leaf (d11) and outer leaf (d10) during the test with input signal FHUIZ-DS0-0038 (scaling factor = 280%).

The maximum and minimum values are highlighted by a circle of the respective colors of the measured output. The similarity between the measured relative displacements of the inner leaf and outer leaf

shows that there was no steel tie failure. The connection between the inner leaf and outer leaf was stable and good.

3.6.2 Dynamic behavior at mid-height

Figure 3.10 presents the peak relative to the base displacement of the test specimen at mid-height against the peak acceleration data (PTA) collected at the concrete block (base) by sensor ***a1***. The displacement data were collected by laser sensors ***d11*** (inner leaf) and ***d10*** (outer leaf) for all thirteen shaking table tests.

A linear trend is observed for the peak relative displacements for PTA smaller than 0.3 g. Based on this, the results are divided into two phases, Linear Phase, and Non-linear Phase. The linear phase consists of the tests with signals up to **FHUIZ-DS0-0017** (scaling factor = 150%). For PTA above 0.3 g, a non-linear trend of the maximum and minimum displacements is observed. The non-linear behavior of the specimen indicates the presence of damage.

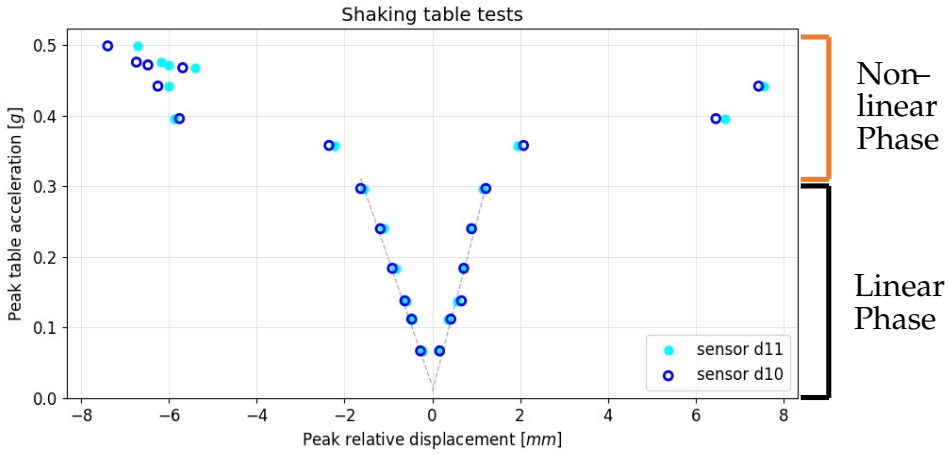

Figure 3.10: Dynamic behavior at the mid-height of the test specimen through the shaking table tests with classification into Linear phase and Non-linear phase.

For the test with signal **FHUIZ-DS0-0020** (scaling factor = 175%), a deviation from the linear trend is observed for the maximum and minimum relative displacements. However, during the experimental test with the above-mentioned signal, no damage was observed. The possible explanation for this deviation could be that the cracking has occurred along the thickness of the outer leaf.

3.6.3 Dynamic behavior over the height

The dynamic behavior was captured using different sensors along the height of the specimen. In Figure 3.11, the evolution of displacement over the height of the specimen, through the sequential application of shaking table tests is presented.

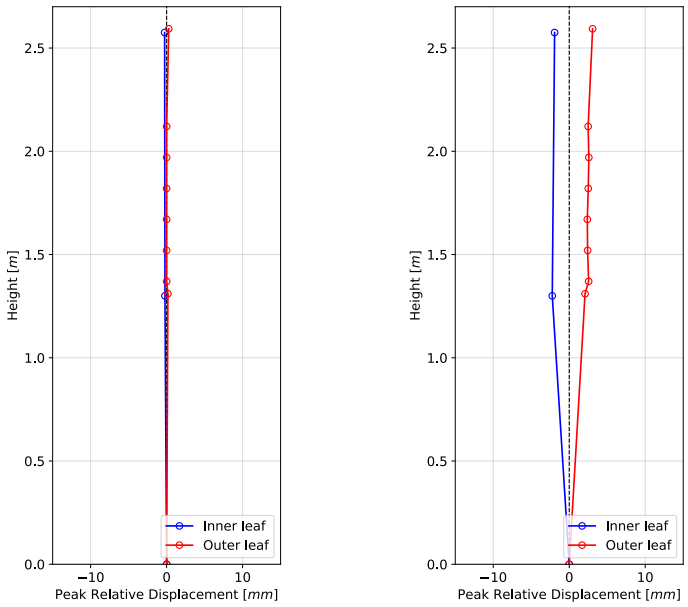

(a) FHUIZ-DS0-0002 (0.03 g) **(b)** FHUIZ-DS0-0020 (0.23 g)

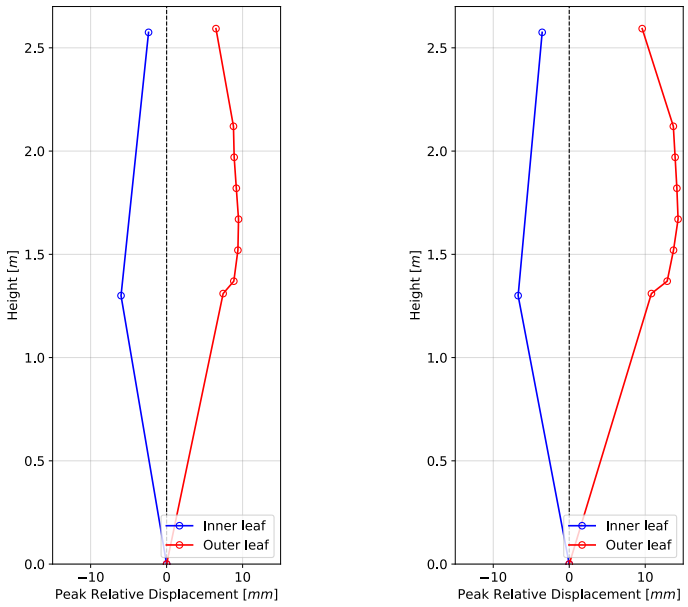

(c) FHUIZ-DS0-0026 (0.29 g) **(d)** FHUIZ-DS0-0038 (0.36 g)

Figure 3.11: Dynamic behavior of the specimen through the shaking table tests. The dynamic behavior is evaluated after the application of the presented input signal Section 3.5.

The maximum relative displacement of the outer leaf and the minimum relative displacement are used to evaluate the evolution. The displacements along the height of the specimen are relative to the displacements of the shaking table.

As described in Section 3.4, the acceleration sensors recorded data at the concrete block, top beam, and three locations along the inner leaf and outer leaf. All the acceleration data obtained from these sensors were processed and filtered. The acceleration data were integrated into velocities and displacements.

The Linear phase of the specimen can be observed from Figure 7.12a to Figure 7.12b. At the test with signal FHUIZ-DS0-0020 (scaling factor = 175%), a small linear deviation was observed Figure 3.10. During the tests, cracking was observed along the 3/4th height of the outer leaf, at the test with signal FHUIZ-DS0-0026 (scaling factor = 200%).

Upon visual inspection of the damage and evaluation of results, the shaking table tests were categorized into their corresponding damage states. The damage states were evaluated on the basis maximum crack width of the cracks. The literature on damage states was presented in Chapter 2. The crack width was evaluated using the DIC technique and postprocessing of the images captured during the tests. The tests were categorized as the following

- Damage State 0 (DS0)- upto test with PTA 0.03 g - No cracking observed.
- Damage state 0 star (DS0*) - Between tests with PTA 0.23 g and 0.29 g - Light damage initiated but cracks hidden within the thickness of the outer leaf.
- Damage state 1 - Tests with PTA more than 0.29 g - Light damage present, cracks with width up to 0.1 mm present.

The numerical models are calibrated on the basis of the shaking table test results. The setup of finite element models is presented in Chapter 5 and the results are presented in Chapter 7.

4 PROCESSING THE OUTPUT OF EXPERIMENTAL TESTS

4.1 INTRODUCTION

Data collected from sensors usually consists of noise and certain errors. The acceleration and laser sensors highlighted in Figure 3.6 collected acceleration and displacement data. The acceleration data collected from the acceleration sensors are plotted against time vectors, thereby creating an acceleration time history. The corresponding time histories of velocity and displacement are calculated using approximated numerical integration methods such as cumulative trapezoidal integration.

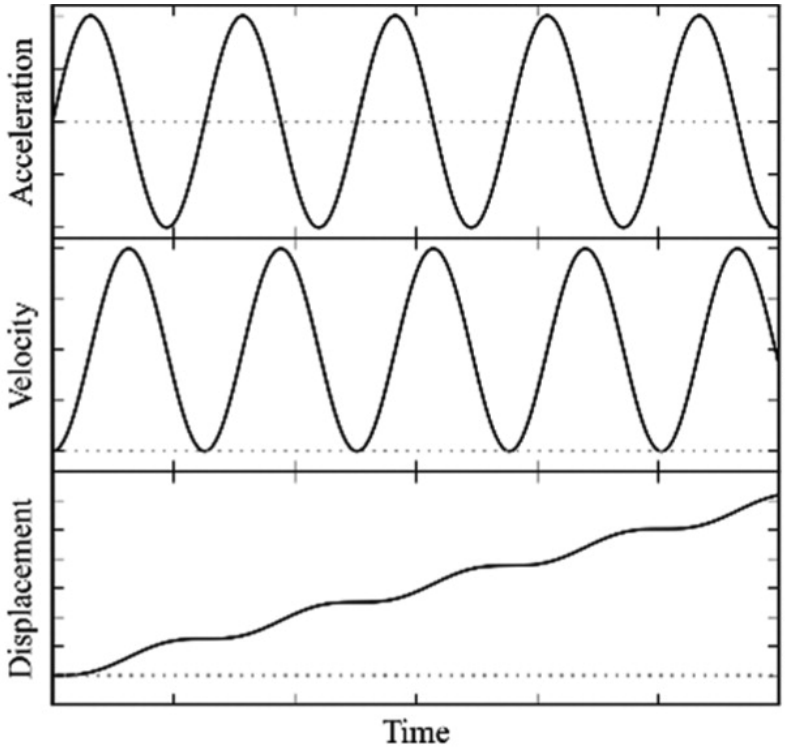

Figure 4.1: A simple demonstration of the phenomenon of baseline drift. The velocity and displacement (assuming v_0=0,d_0=0) curves are obtained by numerical integration of acceleration signal a(t) = A*sin(t). [18]

.

Figure 4.1 demonstrates baseline drift using harmonic waves, where the acceleration signal is $a(t) = A * sin(t)$, where A is the amplitude

of the signal. The acceleration signal is integrated into velocity and displacement using the cumulative trapezoidal integration method. Assuming zero initial conditions (the inconsistent initial conditions), baseline drift is observed with a linear trend. Baseline drift is basically an accumulation of errors as the acceleration signal is numerically integrated over time. Research by [18] highlights, initial values of velocity and displacement must be known in order to obtain accurate time histories. These values are difficult to obtain in real-case scenarios and are usually assumed. This assumption in most cases leads to a phenomenon of baseline drift (drifting of velocity and displacement data). A study conducted by [18] provides a theoretical explanation of what causes the baseline drift phenomenon.

In this chapter, different approaches taken to reduce the effect of baseline drift are discussed. These approaches are applied to the acceleration and displacement data obtained from the shaking table tests. a comparison of these approaches is presented in this chapter to check their efficiency and validity. The goal was to reduce the effect of baseline drift in such a way the raw measured data is not altered to a great extent.

4.2 MEASURED ACCELERATION DATA FROM EXPERIMENTAL TESTS

Acceleration time history data collected from the shaking table tests at the concrete block using sensor a1 is shown in Figure 4.2. A normalized Fourier spectrum of the time history is shown Figure 4.2. This data corresponds to the test with input signal FHUIZ-DS0-0011 (scaling factor = 100%). Since the accelerations after 4.5 *sec* are relatively smaller and have a minor influence on the overall nonlinear behavior of the specimen, in order to save time, the acceleration signal is truncated at 0.5 *sec* to 4.5 *sec*. The truncated measured signal is illustrated in Figure 4.3.

This truncation is beneficial to reduce computational time. For consistency, the same truncation is applied to all the tests. DIANA 10.5 FEA uses approximated numerical integration techniques to evaluate velocities and displacements from input acceleration time histories. In the same figure, Figure 4.3, the corresponding baseline drift trend of the double integrated acceleration signal is also highlighted. Three approaches are explored to reduce this baseline drift trend so that the acceleration signal can be suitable as an input loading for finite element modeling.

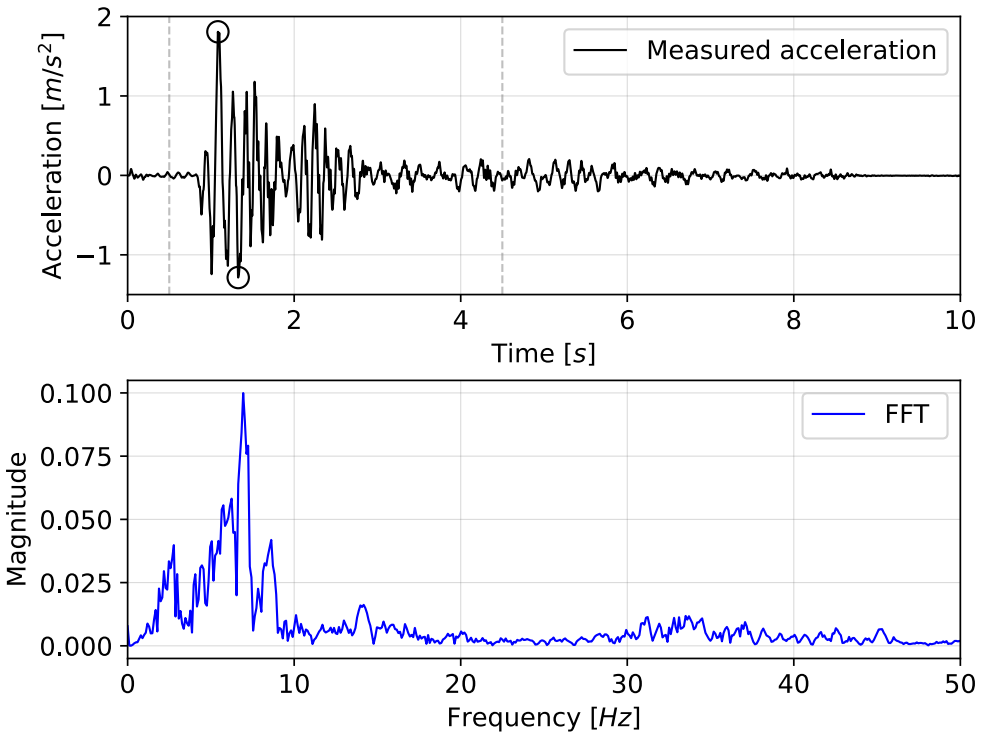

Figure 4.2: Acceleration measured at the concrete block for the test with signal FHUIZ-DSo-0011 (scaling factor = 100%) and its normalized Fourier spectrum.

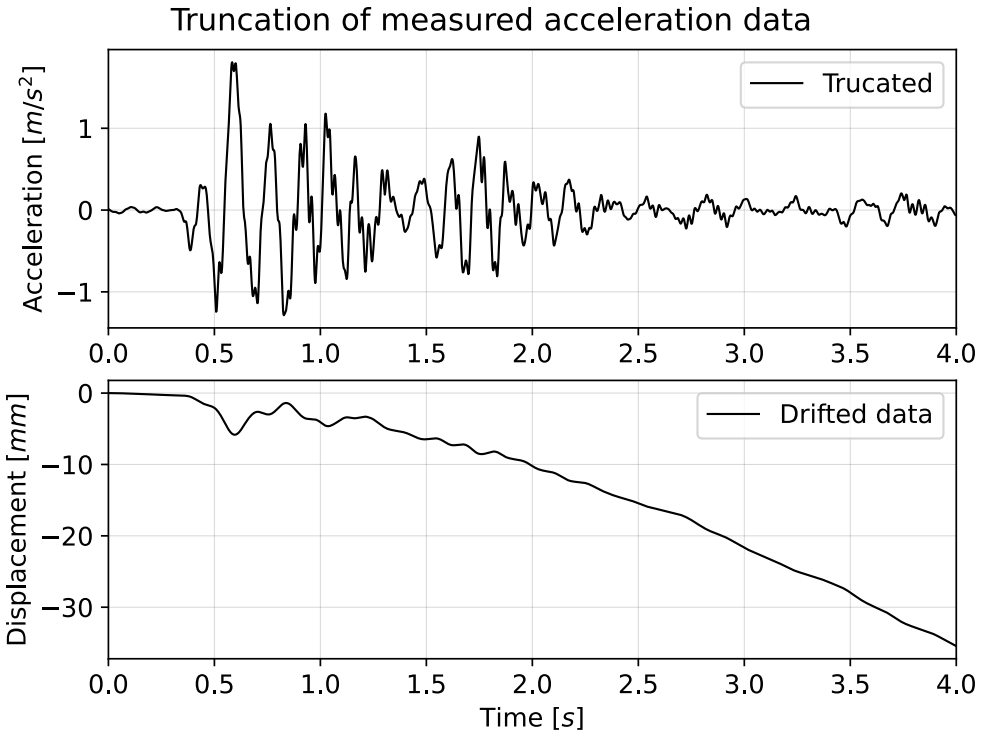

Figure 4.3: Truncation of measured acceleration Figure 4.2 between 0.5 *sec* and 4.5 *sec*. The data is shifted in order to start at 0 *sec*. The double-integrated displacement data of the truncated signal highlights the baseline drift phenomenon.

4.3 APPROACH 1: SMOOTH ENDS

In the first approach, the Tukey window function is applied to the truncated measured acceleration signal. This is to ensure that the signal has smoother end conditions. The Tukey window function is shown in Figure 4.4. The α factor determines the smoothness of the ends.

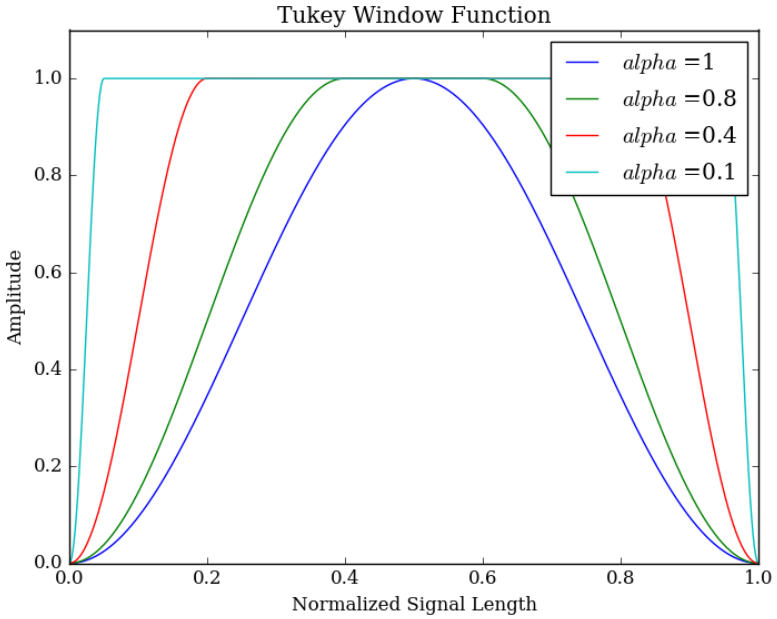

Figure 4.4: Tukey window function for different values of α factor.

Figure 4.5 illustrates the application of the Tukey window to the truncated measured acceleration signal. The baseline drift is still present and needs more elaborate methods for its reduction.

4.4 APPROACH 2: MOVING AVERAGE FILTER

Based on [23], there are several methods available to remove the baseline drift. In this approach, the polynomial curve fitting method is used. The double-integrated drifted displacement data is processed and differentiated to corrected acceleration data. The steps of Approach 2 are presented in Figure 4.6.

The moving average is a common technique used to smoothen out short-term fluctuations in data and highlight long-term trends or patterns. In the context of time history data, a moving average can be used to filter out noise or unwanted variability in the data and make it easier to visualize and analyze the underlying trends or patterns.

Figure 4.7 shows the effect of Approach 2 on the baseline drift. The double-integrated displacement time history follows a baseline drift

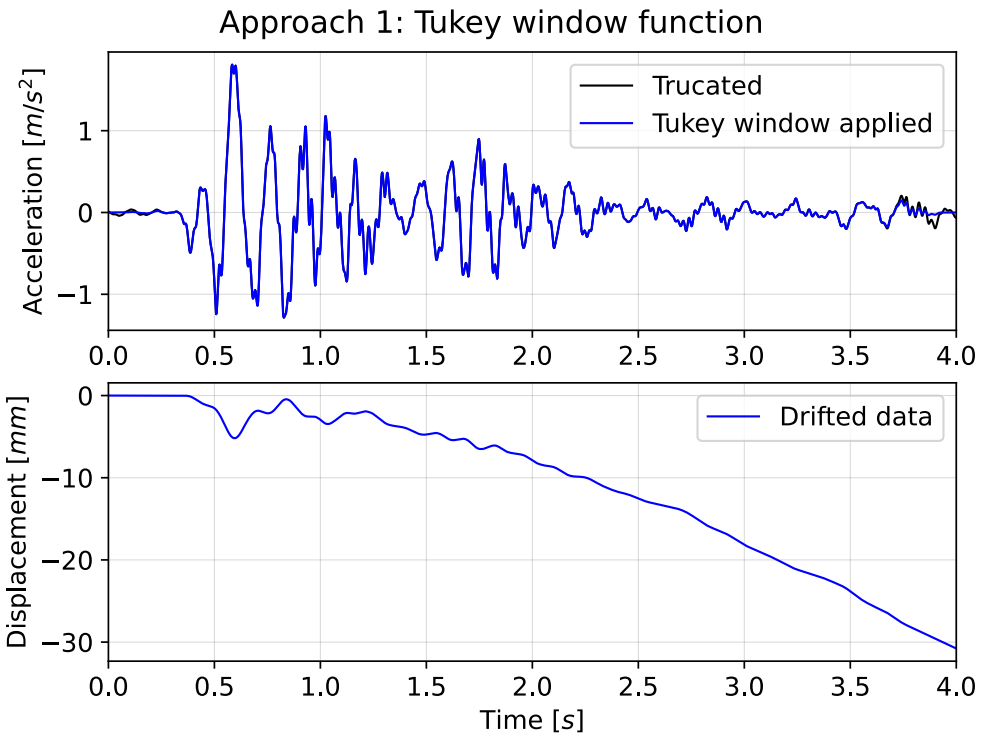

Figure 4.5: Truncated data with Tukey window applied

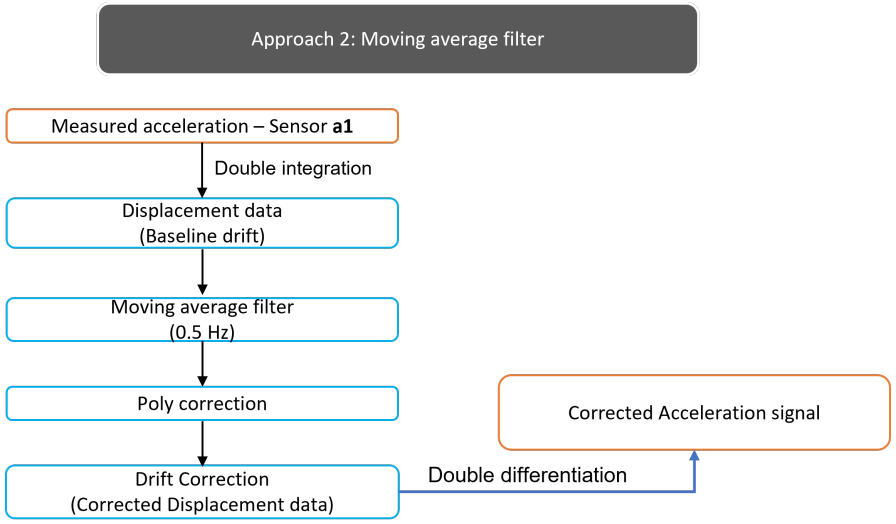

Figure 4.6: Flowchart highlighting the steps of Approach 2: Moving average filter.

(black) along a polynomial trend. The moving average filter (yellow) is used to trace the displacement data and highlight the polynomial trend. The polynomial trend is traced based on the span of values specified (i.e filter frequency) specified.

The highlighted polynomial trend is subtracted from the drifted displacement data, the signal is centered and polynomial trend corrected displacement data (red) is obtained. It was observed that the polynomial corrected displacement data was drifting exponentially

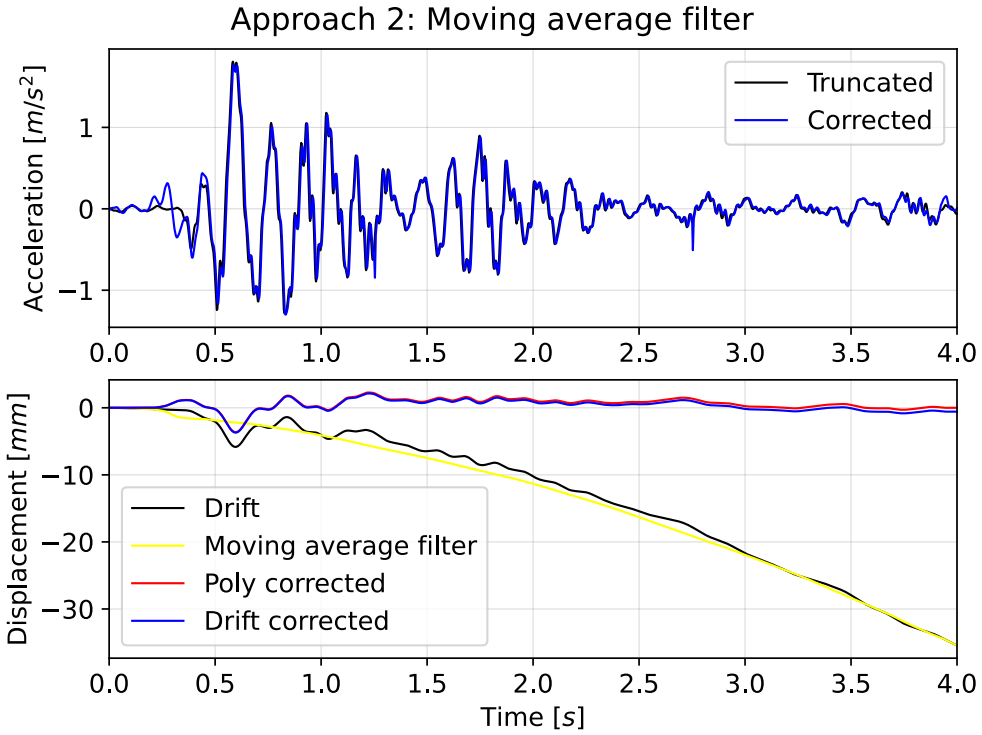

Figure 4.7: Approach 2: Moving average filter applied to truncated data (black) and compared to corrected acceleration signal (blue).

(approximated by a power of 1.2). This was corrected by subtracting the exponential trend. In this way, the drift component is removed from the displacement data. The trend removed and drift corrected displacement data (blue) is differentiated to obtain corrected velocity and corrected acceleration data. This procedure is complex and specific to the properties of the signal.

4.5 APPROACH 3: HIGHER ORDER FILTERS

The baseline drift trend can also be inferred as a low-frequency signal. In this approach, the High-pass frequency domain filtering method is used to remove drift-causing low frequencies. The low frequencies of the signal are removed based on the evaluation of the Fast Fourier transformation (FFT) of the signal. In general, the performance of a filter is characterized by its frequency response, which describes how the filter responds to different frequencies.

In this approach, two filter settings were explored, the Butterworth filter Figure 4.8 and the Chebyshev filter Figure 4.9.

In this method, the low-pass and high-pass filters were applied at separate points. A high pass filter of 5th order with a cutoff frequency of 0.5 Hz is applied to the measured acceleration data before it is numerically integrated.

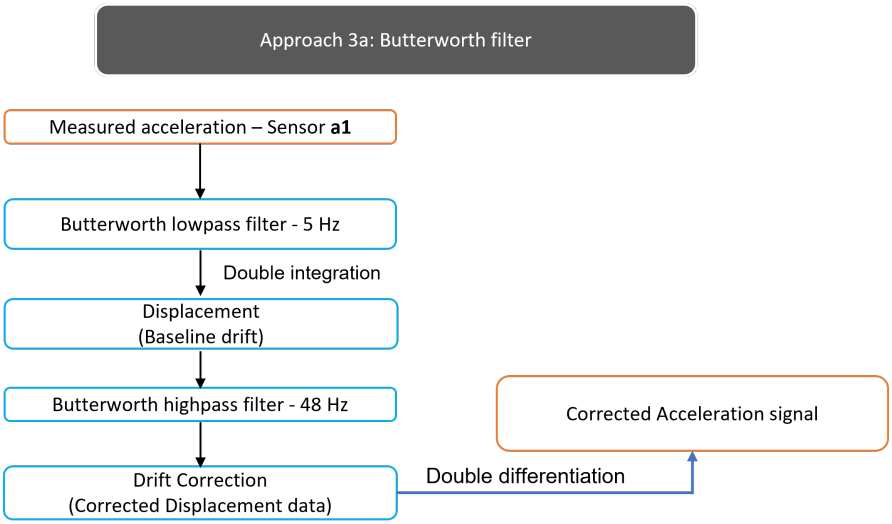

Figure 4.8: Flowchart highlighting the steps of Approach 3a: Butterworth filter.

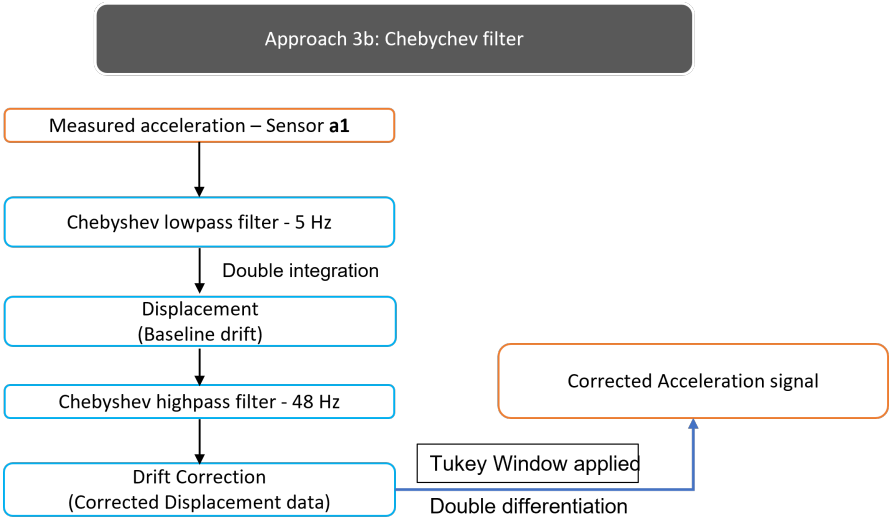

Figure 4.9: Flowchart highlighting the steps of Approach 3b: Chebyshev filter.

In this way, the noise causing high frequencies is removed. The high pass filtered measured acceleration data is numerically integrated into velocities and drifted displacement data. At this point, the low pass filter of 5th order with a cutoff frequency of 48 *Hz* is applied to the drifted displacement data, thereby removing the drift causing low frequencies.

The cutoff frequencies and the order of the filter are kept consistent for both methods for better comparison. The Tukey window is also applied to the drift-corrected displacement data which is differentiated into corrected velocity and acceleration data.Figure 4.10 and Figure 4.11 the baseline drift is corrected. Both approaches give similar results.

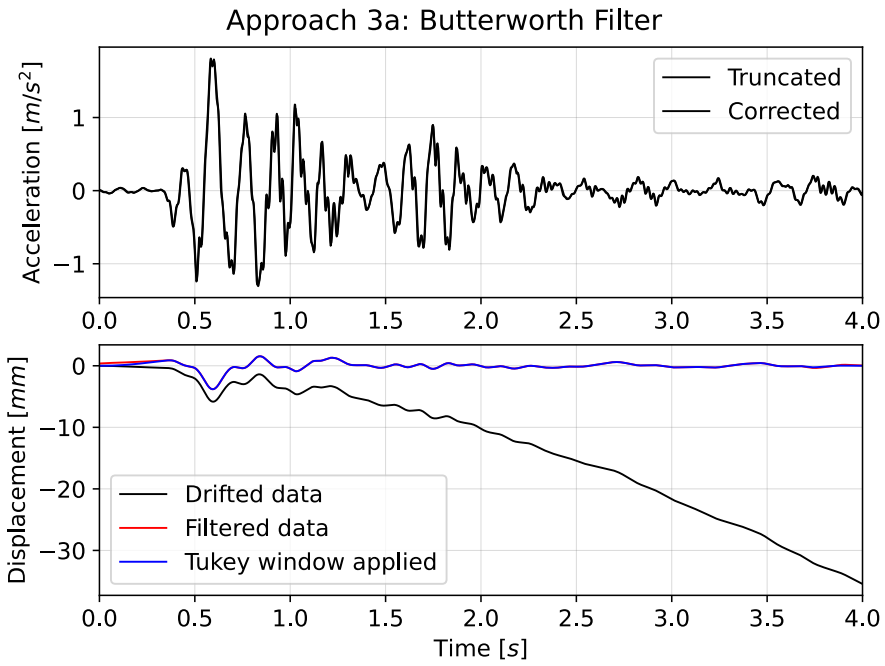

Figure 4.10: Approach 3a: Butterworth filter applied to truncated data (black) and compared to corrected acceleration signal (blue).

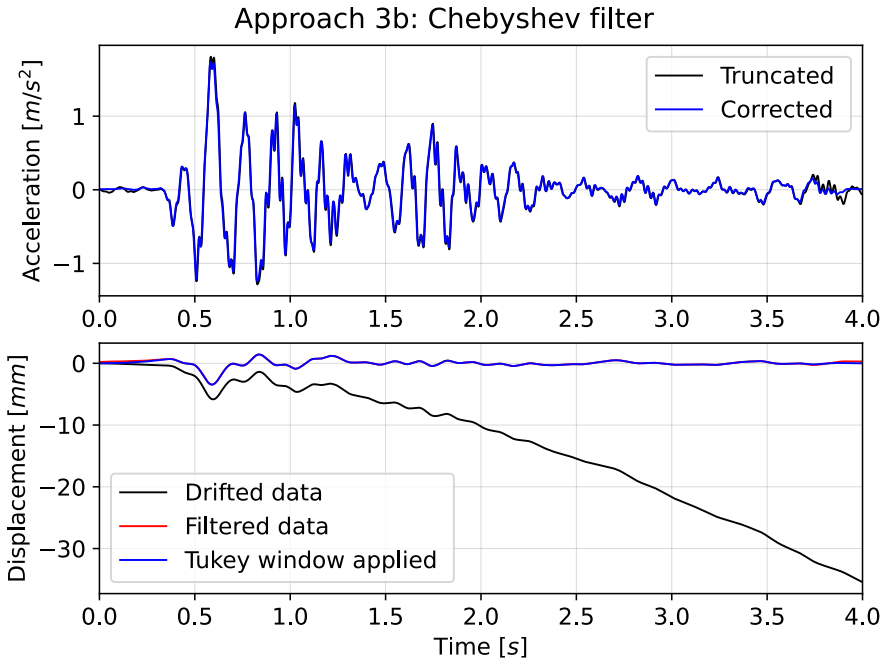

Figure 4.11: Approach 3b: Chebyshev filter applied to truncated data (black) and compared to corrected acceleration signal (blue).

4.6 COMPARISON OF APPROACHES

Three approaches were discussed in the previous sections. As observed, Approach 2 (Moving average filter) and Approach 3 (Higher order filters) reduced the baseline drift substantially. The truncated

acceleration data was also preserved sufficiently in all the approaches.

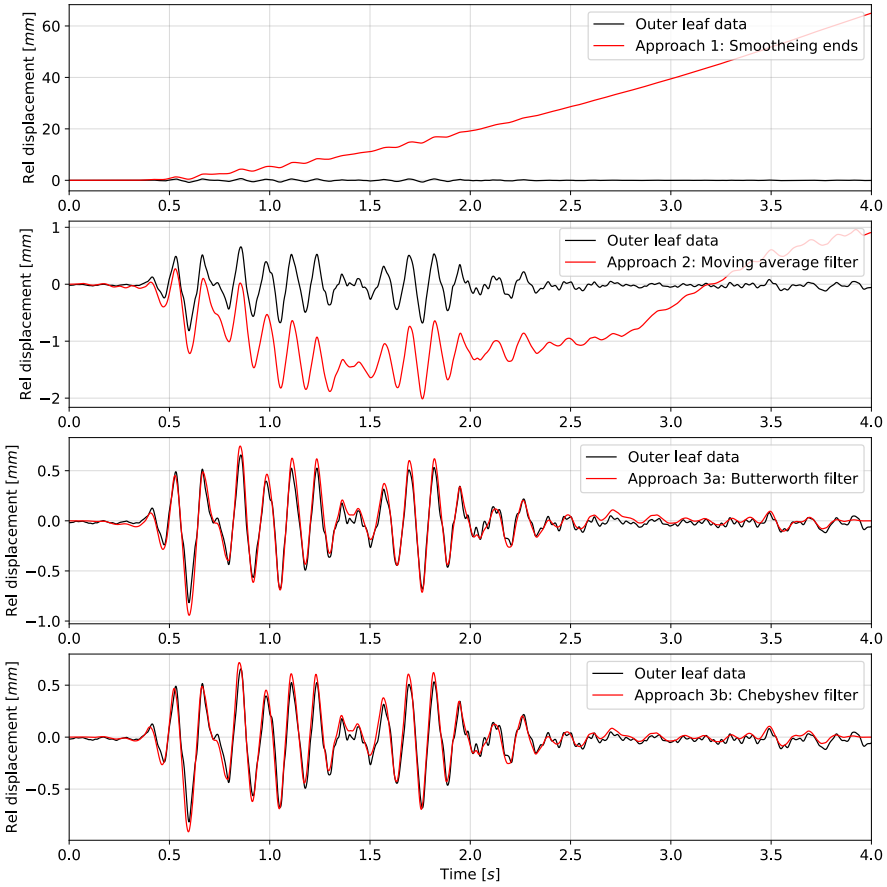

Figure 4.12: Comparison of approaches for outer leaf sensor with (***d10***).

In order to check the validity of the approaches, a comparison is conducted. The sensor positions used for experimental setup, as highlighted in Section 3.4, there are laser sensors and acceleration sensors over the height of the specimen. At the mid-height of the specimen, for the inner leaf as well as the outer leaf, there are laser sensors and acceleration sensors. The laser sensors collect the displacement data of the specimen relative to the base. At the same locations, acceleration data is also collected by the acceleration sensors. The validity of the approaches is checked by deriving relative to base displacements from the acceleration sensors by integrating using the previously described approaches. This data is compared with the relative to the base displacement data obtained from the laser sensors.

For the outer leaf, at mid-height, laser sensor ***d10*** and acceleration sensor ***a4*** are used to collect information. First, the relative to base acceleration of the inner leaf at mid-height is calculated by subtracting the base acceleration collected by sensor a1 from acceleration data collected by sensor ***a4***.

This data is integrated into velocities and displacements by using the three approaches. The double integrated data is therefore relative

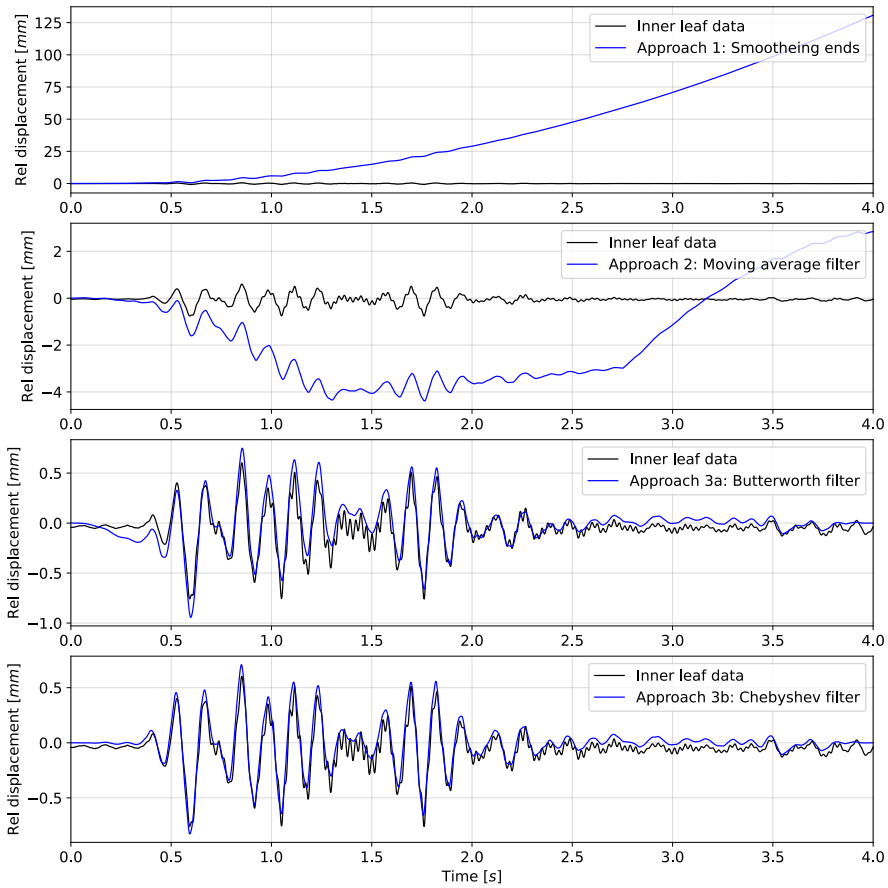

Figure 4.13: Comparison of approaches for inner leaf with (***d11***).

to base displacement data obtained from the acceleration sensors ***a4*** and ***a1***. A comparison of relative to base displacement data, using the three approaches is presented for the outer leaf in Figure 4.12

Similarly, for the inner leaf, the relative to base displacement data obtained from double integration of acceleration data from sensors ***a5*** and ***a1*** is compared to laser ***d11***. The comparison for the inner leaf is presented in Figure 4.13

4.7 INPUT SIGNAL FOR FINITE ELEMENT MODELS

Three approaches were discussed in previous sections for the reduction of baseline drift. These approaches are compared on the basis of relative to the base displacement of the specimen at mid-height. Figure 4.12 and Figure 4.13, present the comparison of the three approaches for the outer leaf and inner leaf.

Approach 1 (Smoothening ends) shows that there is the presence of baseline drift which makes it invalid to be used as an input loading. For Approach 2 (Moving average filter), it was observed that it

requires settings that are specific to the signal. The acceleration signal for all tests should be filtered using the same settings through all thirteen tests for consistency.

Approach 3 (higher order filter), was similar relative to the base displacement data collected by the laser sensors. This approach is valid to be used as an input loading for finite element models. Approach 3: Chebyshev filter suits best the research as the settings used for the postprocessing of the results of shaking table tests also used this approach. Therefore for consistency, the measured acceleration from sensor ***a1*** is filtered using Approach 3b: Chebyshev filter and used as an input loading for the finite element models described in Chapter 5.

5 FINITE ELEMENT MODELING OF URM CAVITY WALL

5.1 INTRODUCTION

To conduct a numerical assessment of the shaking table tests finite element modeling is chosen. In this chapter, the models created in DIANA FEA 10.5, for the URM cavity wall under out-of-plane loading are presented. The finite element model of the test specimen is divided into two Cases on the basis of boundary conditions. The models used for the *Linear Phase* are discussed first followed by the models used in the *Non-Linear Phase*. It is important to note that in this study, the input signals are not sequentially applied.

5.2 CASES OF FEM BASED ON BOUNDARY CONDITION

The test specimen is modeled through the cross-section along the *X-Y plane*. In this way, the behavior of the specimen along the thickness of the inner leaf and the outer leaf could be captured in the finite element modeling. The dimensions of the test specimen which is used for the finite element model is shown in Table 5.1 and Figure 5.1. Two steel ties were used in the experimental setup along the *Z-axis*. The effective diameter is calculated so that two steel ties can be modeled as one. The location and orientation of the steel ties along the height of the specimen correspond to the experimental setup.

Dimensions	Notation	Inner leaf	Outer leaf	Steel ties	Unit
Length	l	1.43	0.1	0.08	m
Thickness	t	0.102	1.335	-	m
Height	h	2.665	2.606	-	m
Effective Diameter	d_{eff}	-	-	0.0051	m

Table 5.1: Dimensions of cavity wall test specimen used for the finite element modeling as shown in Figure 5.1.

In Chapter 3, the boundary conditions of the test specimen undergoing shaking table tests were presented. The URM cavity wall was fixed at the bottom. At the top of the inner leaf, an overburden load was applied using prestressing mechanism and a top beam. This top

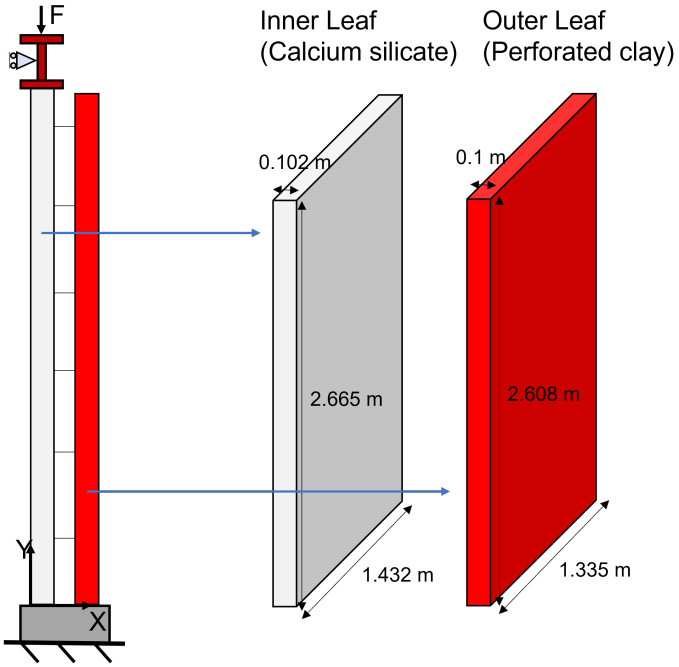

Figure 5.1: Dimensions of the test specimen used in shaking table tests by TNO (2020).

beam was connected to the supporting white frame by using a hinge, which allowed the beam to translate along the *Y-axis* and rotate about its axis freely. Two Cases are explored to compare the effects of this top boundary condition. The two Cases are presented and discussed in this section. The dimensions of the model are consistent in both Cases.

5.2.1 Case 1: Roller boundary condition

Figure 5.2a, shows the analytical model of the experimental setup and the finite element model used. The analytical model is along the *X-Y plane* of the test specimen thereby highlighting the thickness of the inner and the outer leaf. The finite element model for Case 1 shown in Figure 5.2b is developed on the basis of this analytical model.

The inner leaf and outer leaf were modeled using 4-noded quadrilateral isoparametric plane stress elements (Q8MEM). The stresses along the *Z-axis* i.e σ_{zz} are considered to be zero. The steel ties are modeled as 2 - noded isoparametric beam elements (L6BEA) instead of spring elements for simplicity. The elements used for modeling the URM cavity wall are highlighted in Figure 5.3.

The cavity wall is fixed at the bottom. To simulate the fixed condition at the bottom, tying is used. This master node for the bottom boundary condition is located at the bottom left corner node, *Node 9*, which is fixed along *X-axis* and *Y-axis*. The rest of the bottom nodes of the inner leaf and outer leaf are tied to this master node. This enables

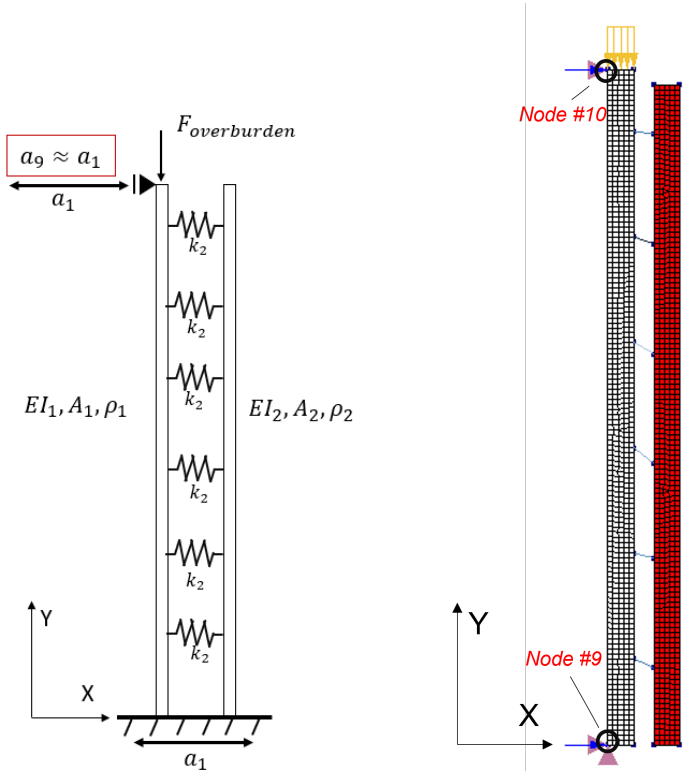

(a) Analytical model **(b)** Case 1 finite element model

Figure 5.2: Analytical model of the experimental setup and its corresponding finite element model for Case 1: Roller boundary condition.

all the nodes at the bottom to have the same displacement during the analysis.

	Q8MEM		T6MEM		L6BEA
	Inner leaf	*Outer leaf*	*Inner leaf*	*Outer leaf*	*Steel Ties*
Integration scheme	$u_i(\xi,\eta) = a_0 + a_1\xi + a_2\eta + a_3\xi\eta$		$u_i(\xi,\eta) = a_0 + a_1\xi + a_2\eta$		$u_x(\xi) = a_0 + a_1\xi$ $u_y(\xi) = b_0 + b_1\xi$ $\phi_z(\xi) = c_0 + c_1\xi$
Mesh size	0.01 m		0.01 m		0.01 m
Element thickness	1.432 m	1.335 m	1.432 m	1.335 m	Φ = 0.0051 m
Number of nodes					
Number of elements	667	654	1	2	26

Table 5.2: Descriptions of finite elements used in Case 1: Roller boundary condition.

In Case 1, the top boundary condition at the inner leaf is simulated using roller support. This is a simplification of the experimental setup by avoiding modeling the top beam and its connection to the white supporting frame as highlighted in the Chapter 3.

A tying condition is used for the top boundary condition as well. The master node is at the left top corner, *Node 10*, and all the top nodes of the inner leaf are tied to this node. The top nodes of the inner leaf were fixed along *X-axis*, whereas the *Y-axis* and the rotation

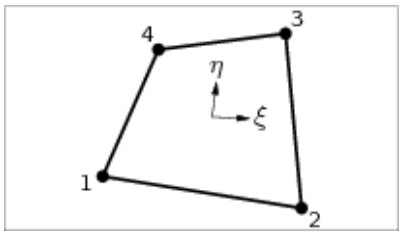

(a) 8-noded quadrilateral element

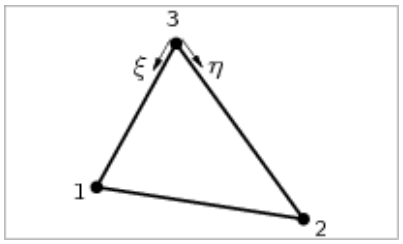

(b) 3-noded triangular element

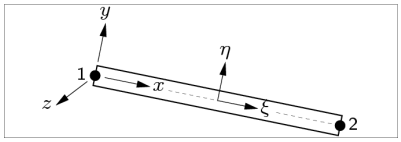

(c) 2-noded beam element

Figure 5.3: Types of elements used for Case 1: Roller boundary condition.

were allowed. The overburden load (21 kN)on the inner leaf was represented by a uniformly distributed force of 205882.35 N/m over the thickness of 0.102 m.

5.2.2 Case 2: Spring mass boundary condition

In the experimental test results for displacement over the height of the specimen, it was observed that the top of the inner leaf was able to translate in the *X-axis*.

To highlight this behavior, instead of roller support, the spring-mass support is used to replicate the top boundary condition. The spring represents the hinge that connects the top beam to the white support frame. The analytical model of Case 2 is shown in Figure 5.4a. The finite element model of Case 2 is developed on the basis of this characterization. The model properties are similar to Case 1 with an updated top boundary condition at the inner leaf.

The top beam (300 kg) is modeled as a distributed line mass element of mass 2941.2 kg/m, over the thickness of 0.102 m. This enabled consistent distribution of the mass in the nodes along the thickness of the inner leaf. It is important to note that the line mass element only adds to the structural mass of the model and does not affect its static behavior, thereby only affecting the inertial effects. The types of elements used for the top boundary condition in Case 2 are shown in Figure 5.5.

A dummy node was created at 0.3m away from the top node of the inner leaf towards the negative *X-axis*. A spring connection was used to connect this dummy node, *Node 808*, and the distributed line mass at *Node 10*.

The top beam in the experimental setup was allowed to rotate, the behavior is captured in the numerical model by tying the nodes of

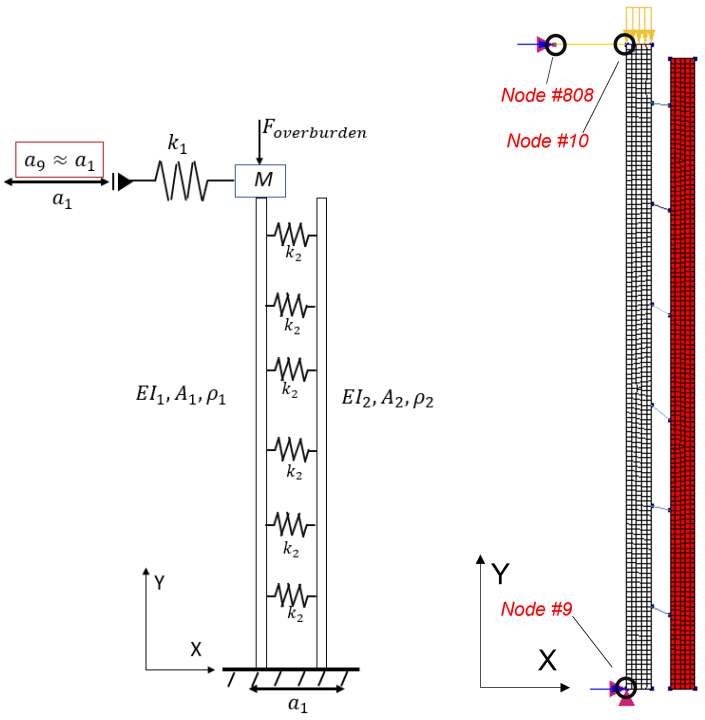

(a) Analytical model **(b)** Case 2 finite element model

Figure 5.4: Analytical model of the experimental setup and its corresponding finite element model for Case 2: Spring mass boundary condition.

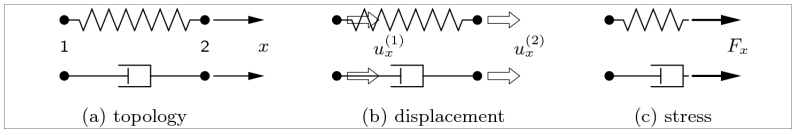

(a) Spring connection

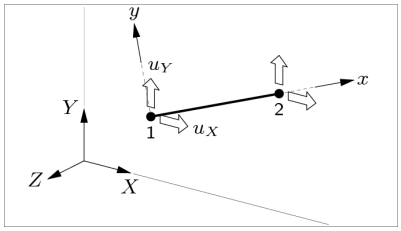

(b) Mass element

Figure 5.5: Elements used for top boundary condition in Case 2: Spring mass boundary condition.

the line mass to *Node 10* only along *X-axis*. This allows the line mass to move freely along the *Y-axis*. The nodes at the bottom edge of the model are fixed in *X-axis* and *Y-axis* similar to Case 1.

5.3 FINITE ELEMENT MODELING OF LINEAR PHASE

The shaking table test results were characterized into two phases, Linear and Non-linear phase. This differentiation was discussed in previous Chapter 3 in Section 3.6.2. The finite element models are classified into Linear phase and Non-linear phase on the basis of input seismic signal. In this section, the models used for the *Linear Phase* are presented.

5.3.1 Input seismic signal for Linear Phase models

In this study, unlike the shaking table tests, the input seismic signals are not applied sequentially to the models. The first six shaking table tests of the experimental setups correspond to the *Linear Phase*. For the *Linear Phase*, six models were created Table 5.3, corresponding to the input seismic signal for Case 1 and separately for Case 2 as well.

Model name	Input seismic signal	Top boundary condition	
		Case 1: Roller	*Case 2: Spring mass*
Model 1	FHUIZ-DS0-0002	Yes	Yes
Model 2	FHUIZ-DS0-0005	Yes	Yes
Model 3	FHUIZ-DS0-0008	Yes	Yes
Model 4	FHUIZ-DS0-0011	Yes	Yes
Model 5	FHUIZ-DS0-0014	Yes	Yes
Model 6	FHUIZ-DS0-0017	Yes	Yes

Table 5.3: Finite element models corresponding to the *Linear Phase* on the basis of input seismic signal Section 3.5.

Acceleration sensors were used to capture the acceleration data over the height of the specimen. The acceleration sensor ***a1*** Figure 5.6, measured the acceleration data at the concrete block of the test specimen. This raw measured data was processed Chapter 4 and applied as an input seismic signal for the finite element models of the *Linear Phase*. It assumed for simplicity that the test specimen experiences the same seismic excitation at the top as well as the bottom.

For Case 1, Figure 5.2, the input seismic signal was applied to the top and bottom boundary conditions using acceleration control. The acceleration control was applied to the master node *Node 9* at the bottom and at the master node at the top *Node 10*. This ensured that the model experienced the same seismic excitation at the top and the bottom simultaneously thereby replicating the experimental shaking table tests.

Similarly, for the *Linear Phase* models of Case 2, Figure 5.4, acceleration control was used for the input seismic signal. The bottom nodes experienced seismic excitation by applying acceleration control at the master node at the bottom. The difference in Case 2 was that the acceleration control at the top was applied to the dummy node, *Node 808*

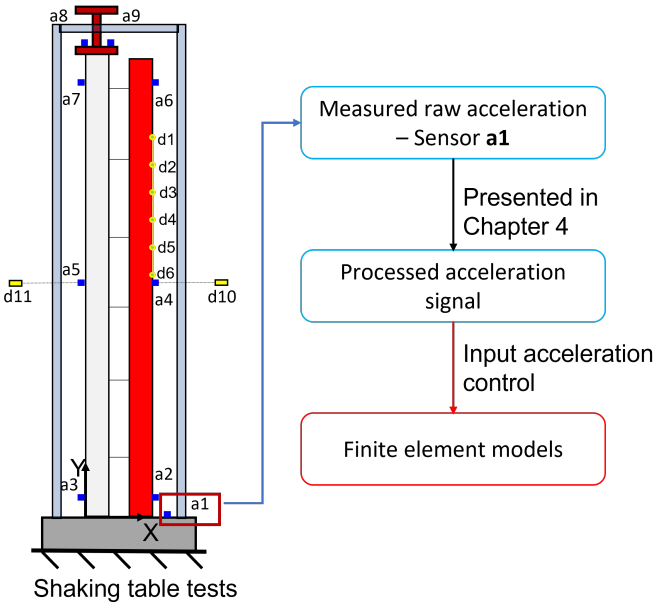

Figure 5.6: Process of application of input seismic signal to the finite element models.

which was connected to the distributed line mass by using a spring connection.

5.3.2 Linear elastic material properties

Based on the experimental results, no non-linear behavior or cracking was observed during the *Linear Phase*, therefore it can be assumed that the cavity wall behaves linear elastic up to test with signal **FHUIZ-DS0-0017** (scaling factor = 150%). To check the validity of the models in the *Linear Phase*, transient analysis was conducted with elastic material properties. The linear properties adopted are shown in Table 5.4. These properties are calculated using EUROCODE 6 [1] and NPR998:2020 .

Material properties	Notation	Inner leaf	Outer leaf	Steel ties	Unit
Young's modulus	E	9658.3	8050	210000	N/mm^2
Poisson's ratio	μ	0.22	0.17	0.3	-
Mass density	ρ	1890	1587	8000	kg/mm^3

Table 5.4: Linear material properties calculated using EUROCODE 6 [1] and NPR998:2020

Young's modulus calculated is of the masonry of the inner leaf and outer leaf homogenized. The mass density calculated is based on the total mass of the test specimen. This does not include the mass of the top beam and the concrete block.

5.3.3 Preliminary eignevalue analysis

A preliminary eigenvalue analysis was conducted to identify the dynamic properties of the finite element models. This analysis was conducted on both Case 1 and Case 2. Hammer tests were conducted on the test specimen by TNO Chapter 3. Based on the hammer tests, it was found that the first natural frequency of the test specimen was 10.9 Hz and the second natural frequency was 27 Hz. The damping ratio was calculated to be 3.5%.

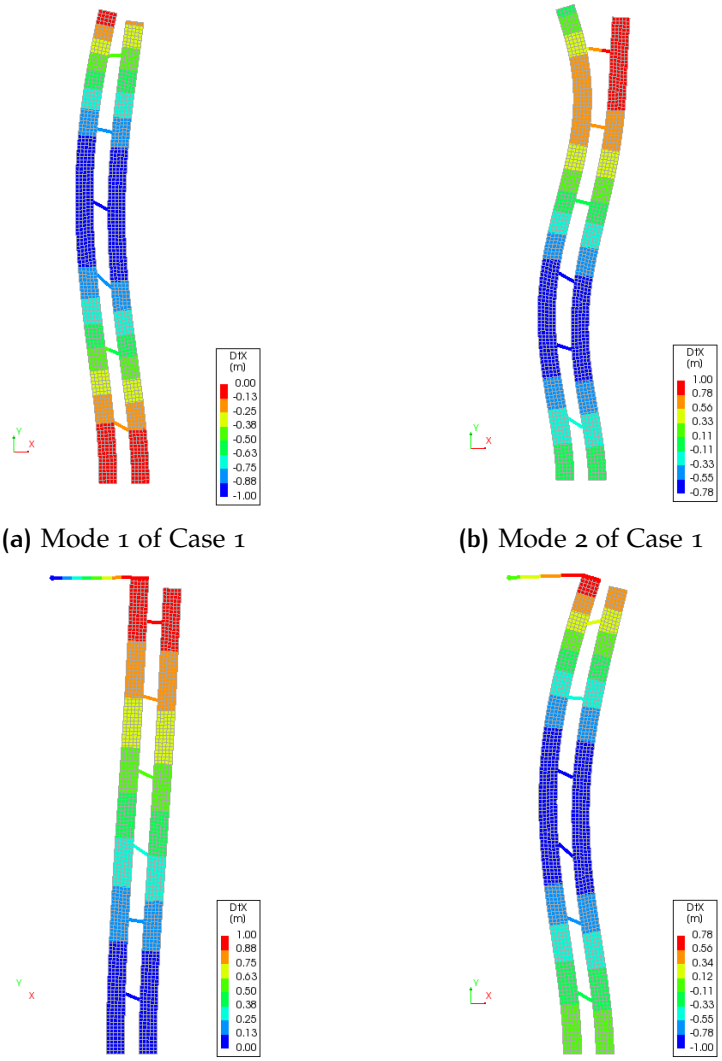

(a) Mode 1 of Case 1

(b) Mode 2 of Case 1

(c) Mode 1 of Case 2

(d) Mode 2 of Case 2

Figure 5.7: Modes and Eigenfrequencies of Case 1 and Case 2

Modes	Eigenfrequencies Hz		
	Case 1	Case 2	Hammer tests
1	22.5	11	10.9
2	67.6	27.4	27.5

Table 5.5: Summary of eigenvalues calculated for the *Linear Phase*.

The Rayleigh damping parameters of the finite element models were evaluated based on these first two frequencies and the damping ratio calculated by the TNO. The damping parameters were found to be; α factor for the mass matrix was 3.4189 s^{-1} and β factor for the stiffness matrix was 0.00029318 s. The summary of the eigenfrequency analysis is presented in Table 5.5. For Case 1, it was observed that the eigenvalues were quite higher than the ones observed in the experimental tests. The explanation for this behavior was the stiff top boundary conditions and the lack of mass of the top beam in the finite element model. Whereas for Case 2, the stiffness of the spring connection was calibrated to match the first natural frequency of the hammer tests. Based on this calibration, the eigenfrequencies obtained were quite similar to the eigenfrequencies of the hammer tests.

5.3.4 Transient analysis for the Linear Phase

Transient analysis for the *Linear Phase* models of Case 1 and Case 2 was performed. Consistent mass and damping matrices were used with no additional numerical damping. The analysis consisted of start steps and time steps. The start step introduced the self-weight and overburden load. The input seismic signal was applied using time steps. The step size was considered to be 0.002 s. The transient analysis scheme used the Implicit Newmark method (default values of DIANA FEA 10.5) and is summarised in Table 5.6.

Parameters	Start Steps	Time Steps
Load Set	Overburden and self weight	Input seismic signal
Iterative scheme	Secant Quasi Newton (BFGS)	Secant Quasi-Newton (BFGS)
Max iterations	10	50
Convergence norm	Displacement: 10^{-2} Force: 10^{-2}	Energy: 10^{-4} Force: 10^{-2}

Table 5.6: Transient analysis settings for the *Linear Phase*.

Measured displacement output

The *Linear Phase* models of Case 1 and Case 2 were seismically excited by using acceleration control at the top and bottom of the specimen. The input seismic signal was processed before being applied as an acceleration control to the finite element models.

This was presented in Chapter 4. Figure 5.8 presents the seismic signal that was applied to Model 4. The displacement is measured at the nodes of application, and no baseline drift phenomenon was observed.

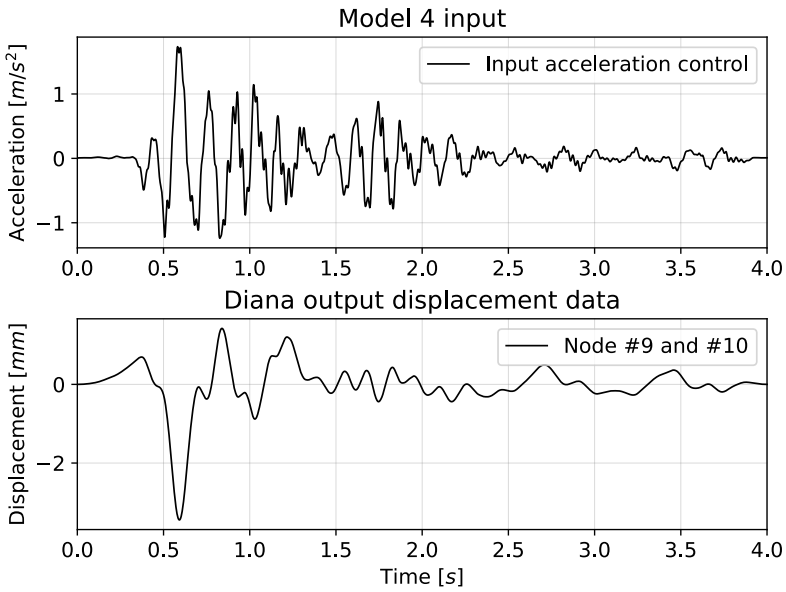

Figure 5.8: Input seismic signal for models corresponding to test FHUIZ-DSo-0011 (scaling factor = 100%) and displacement output measured at the nodes of application, *Node 9* and *Node 10*.

5.4 FINITE ELEMENT MODELING OF THE NON-LINEAR PHASE

In this section, the finite element models used to represent the *Non-Linear Phase* are presented and discussed. The dynamic properties of the *Linear Phase*, for Case 1, did not match that of the experimental tests. The eigenfrequencies obtained for Case 1 were higher than the ones calculated from hammer tests conducted on the test specimen. Based on this, the *Non-Linear Phase* models were created only for Case 2: Spring mass top boundary conditions. For the analysis of the *Non-Linear Phase*, a non-linear material model is chosen, Engineering Masonry Model (EMM).

5.4.1 Input seismic signal for the Non-Linear Phase models

The nonlinear behavior of the test specimen was observed from the shaking table test with input signal FHUIZ-DS0-0020 (scaling factor = 175%). The shaking table tests of the experimental setups shown in Table 5.7 correspond to the *Non-Linear Phase*. The seven models are created on the basis of their input seismic signal only. The input acceleration control for the *Non-Linear Phase* was applied as shown in Figure 5.6.

Model name	**Input seismic signal**	**Top boundary condition**	
		Case 1: Roller	***Case 2: Spring mass***
Model 7	FHUIZ-DS0-0020	No	Yes
Model 8	FHUIZ-DS0-0023	No	Yes
Model 9	FHUIZ-DS0-0026	No	Yes
Model 10	FHUIZ-DS0-0029	No	Yes
Model 11	FHUIZ-DS0-0032	No	Yes
Model 12	FHUIZ-DS0-0035	No	Yes
Model 13	FHUIZ-DS0-0038	No	Yes

Table 5.7: Finite element models corresponding to the *Non-Linear Phase* on the basis of input seismic signal Section 3.5.

5.4.2 Engineering Masonry Model

To simulate the quasi-brittle behavior of the masonry, DIANA FEA 10.5's orthotropic material model Engineering Masonry model was chosen. The constitutive laws of the Engineering Masonry material model will be briefly discussed in this section. The smear cracking idea serves as the foundation for the engineering masonry model. It takes into account the masonry's anisotropy, which is caused by differences in stiffness between the bed joints and head joints. On the

element's plane, there are four predetermined cracks: one in the bed joint direction, one in the head joint direction, and two diagonal directions. An assumed secant nonlinear unloading and reloading behavior is used to analyze the tensile crack in the direction which is either normal to the bed joint or to the head joint.

In order to replicate the extremely nonlinear behavior of the brickwork, the crushing is also evaluated in the direction normal to the bed joint or to the head joint, and the unloading and reloading behavior is considered to be non-secant. The standard Coulomb friction failure criterion forms the basis for the shear failure mechanism.

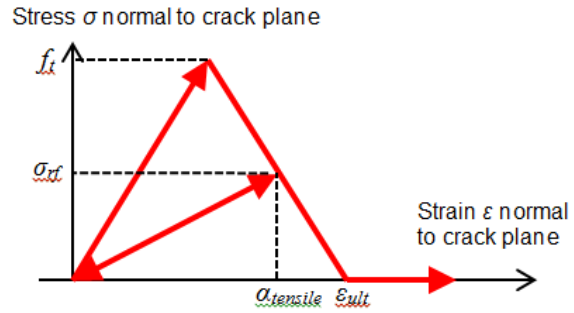

(a) Cracking behavior

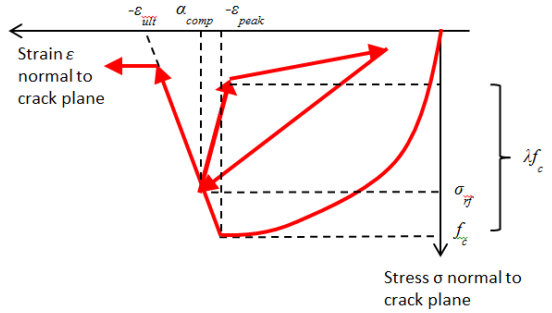

(b) Crushing behavior

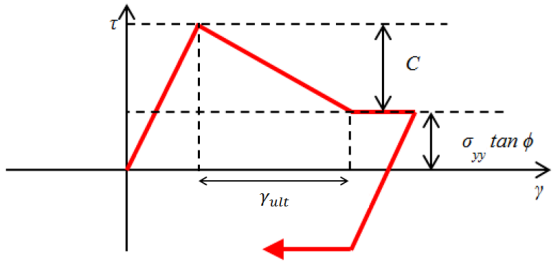

(c) Shear behavior

Figure 5.9: The constitutive laws for Engineering Masonry model in tensile cracking, compressive crushing and shearing [8].

Figure 5.9 presents the constitutive equations for the Engineering Masonry model's tensile cracking, compressive crushing, and shear behavior. By combining severe stress decay with the initial linear stiffness, it more accurately reflects the unloading behavior. The ap-

plication of this model is highly advised for static nonlinear cyclic or transient dynamic nonlinear evaluations of individual components and the entire structure[8].

Paramters	Notation	Inner leaf	Outer leaf	Unit
Elastic parameters				
Modulus of Elasticity	E_x	9658.276	8049.556	N/mm^2
Modulus of Elasticity	E_y	9658.276	8049.556	N/mm^2
Shear modulus	G_xy	3958.31	3439.981	N/mm^2
Mass Density	ρ			kg/m^3
Cracking Parameter				
Bed joint tensile strength	$f_{ma;x;1;m}$	0.208	0.195	N/mm^2
Fracture energy in tension	Gf_t	0.01353	0.012933	N/mm
Crushing paramters				
Compressive strength	$f_{ma;m}$	13.79754	11.49937	N/mm^2
Fracture energy in compression	Gf_c	20.2476	19.46868	N/mm
Factor to strain at compressive strength		4	4	
Unloading		secant	secant	
Shear failure parameters				
Bed joint shear friction coefficient	$\nu_{ma;m}$	0.6	0.75	
Friction angle		0.5401	0.6432	
Cohesion coefficient		0.312	0.2925	N/mm^2
Fracture energy in shear	Gf_v	0.1	0.2	N/mm

Table 5.8: Parameters for Engineering Masonry Model calculated using EUROCODE 6 [1] and NPR 998:2020 .

The parameters required for the Engineering Masonry model pertaining to this study were evaluated using material tests, EUROCODE [1] and NPR 998:2020 . An overview of these parameters is shown in Table 5.8.

5.4.3 Preliminary Eigenvalue analysis

The difference between the models of the *Linear Phase* and the *Non-Linear Phase* is the the use of Engineering masonry model. By making this change, the dynamic properties of the model were not affected. The preliminary eigenvalue analysis showed consistent results as shown in Figure 5.7c and Figure 5.7d.

5.4.4 Transient analysis for the Non-Linear Phase

The transient analysis takes into account both geometrical non-linearity and physical non-linearity. No additional numerical damping is added because the Rayleigh damping is already incorporated into the struc-

ture. In the start step of each model, the self-weight and the overburden load are applied, and then the seismic acceleration signal with a 4-second duration is applied. The setting for the transient analysis for Non-linear phase models are shown in Table 5.9.

Parameters	Start Steps	Time Steps
Load Set	Overburden and self weight	Input seismic signal
Iterative scheme	Secant Quasi Newton (BFGS)	Secant Quasi-Newton (BFGS)
Max iterations	10	50
Convergence norm	Displacement: 10^{-2} Force: $2 * 10^{-2}$	Energy: $5 * 10^{-4}$ Force: 10^{-2}

Table 5.9: Transient analysis settings for the *Non-Linear Phase*.

In order to obtain convergence of results for models with peak table accelerations (PTA) higher than 0.3 g, some changes were made to the default settings. The energy convergence norm has high accuracy. Due to this, the energy norm does not converge at intervals where the seismic signal has an acceleration time history closer to zero. In order to circumvent this problem, force norm was enabled for the time steps. This ensured reliable and converged results.

6 PROCESSING THE OUTPUT OF FEM

6.1 INTRODUCTION

As discussed in chapter Chapter 5, transient analysis was conducted on finite element models. In this chapter, the analysis methods used to evaluate the results of the finite element models are presented. The anal

6.2 DYNAMIC BEHAVIOR AT THE MID-HEIGHT: LINEAR ELASTIC PROPERTIES

Laser sensors ***d11*** and ***d10*** collected the displacement data at the mid-height of the specimen for the inner leaf and the outer leaf respectively. The displacement data was relative to the base motion of the shaking

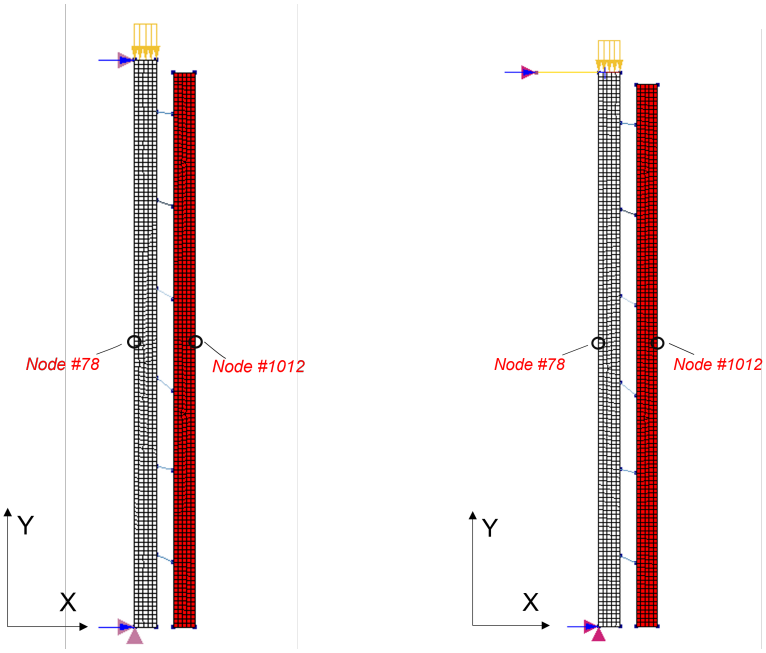

(a) Case 1: Roller support condition

(b) Case 2: Spring-mass support condition

Figure 6.1: Nodes of interest for evaluating the dynamic behavior at the mid-height. The nodes shown here correspond to the laser sensors at mid-height of the test specimen shown in Figure 1.2.

table. The exact locations of the sensors are represented in Figure 1.2. The dynamic behavior of the finite element models at mid-height is evaluated and compared to the experimental shaking table tests. Figure 6.1 shows the nodes of interest in the finite element models where this behavior is evaluated.

Node 78 for the inner leaf and *Node 1012* correspond to the sensor ***d11*** and ***d10*** locations in the finite element model respectively. The dynamic behavior of the specimen at mid-height is assessed for both top boundary cases. As the same geometry and meshing properties were used for both models, the nodal location stayed consistent. The displacement results obtained from *Node 78* and *Node 1012* are used for comparison of the dynamic behavior. The relative to base displacements were evaluated on these locations by subtracting the displacements of the base node (*Node 9*) which corresponded to the sensor ***a1*** on the concrete block.

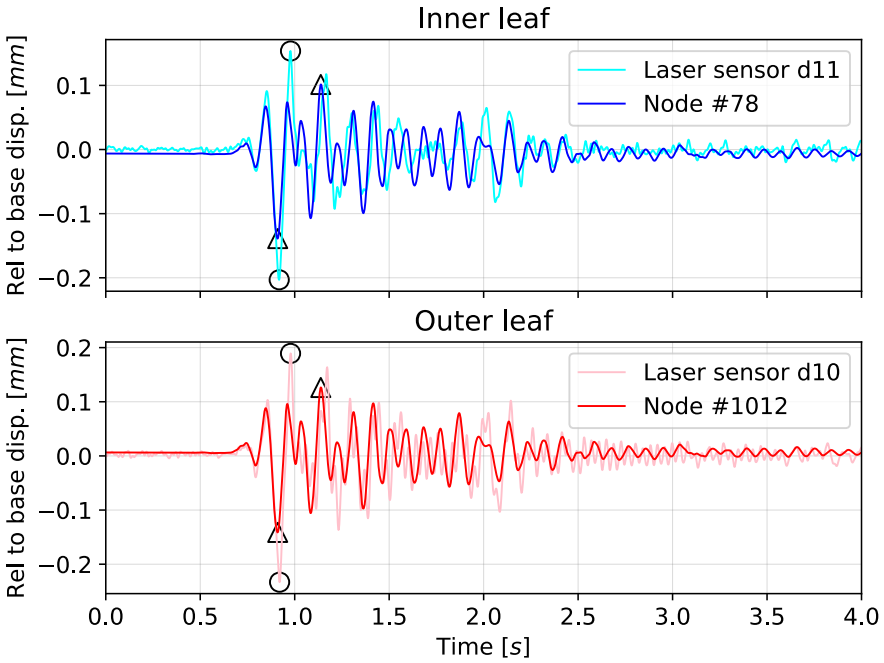

Figure 6.2: Evaluation of maxima of outer leaf and minima of inner leaf for Model 1. Results from FEM are compared to laser sensors used for experimental setup highlighted in Figure 1.2

The calculated relative to base displacements at *Node 78* and *Node 1012* are compared to the laser sensor data of ***d11*** and ***d10*** respectively. Figure 6.2 presents the comparison of relative to displacement data for **Model 1** and its corresponding shaking table test with input signal **FHUIZ-DS0-0002** (scaling factor = 25%). The results are evaluated using linear elastic material properties. The peak values of shaking table results and FEM results are highlighted using a circle and triangle respectively.

6.3 DYNAMIC BEHAVIOR AT THE MID-HEIGHT: EMM PROPERTIES

The method of analysis used for this section is the same as the one described in **??**. On the basis of the results obtained using the linear elastic material properties, the models with Case 1 top boundary condition (roller support) showed to be much stiff than the experimental shaking table test results.

The results presented in the following sections will be evaluated only from the models with Case 2 as the top boundary condition (spring-mass support). Furthermore, the Linear phase, Models 1 to 6 were reanalyzed using the engineering masonry model as the material parameters. This enabled numerical assessment of the nonlinear behavior of the shaking table tests.

6.4 DYNAMIC BEHAVIOR OVER THE HEIGHT: EMM PROPERTIES

The data for dynamic behavior over the height was collected using acceleration sensors. The locations of the acceleration sensors are shown Figure 1.2. The acceleration data gathered from these sensors was filtered and integrated using the Chebyshev filter by TNO to obtain displacement data corresponding to sensor locations. The relative to base displacement data was calculated by subtracting the displacement time history of the shaking table.

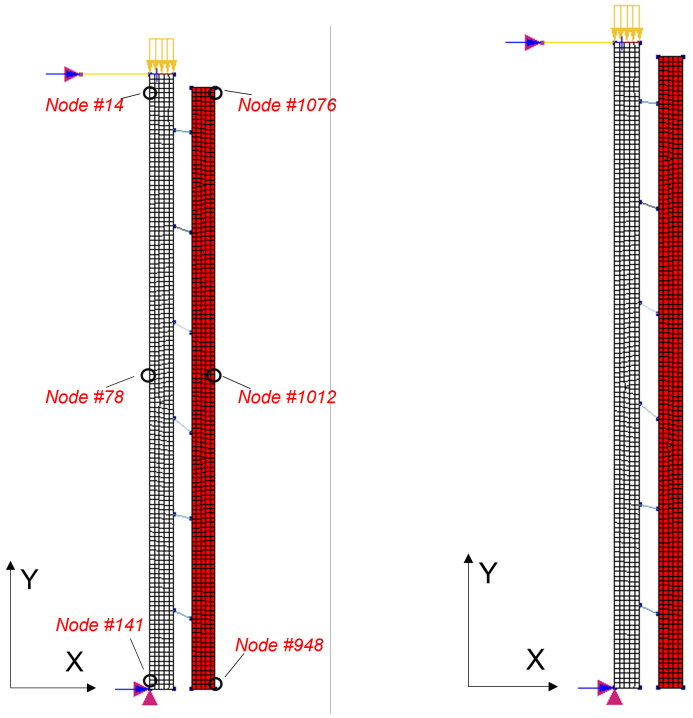

(a) Node of interests corresponding to acceleration sensors.

(b) Nodes of interest corresponding to laser sensors for DIC.

Figure 6.3: Nodes of interest for evaluating the dynamic behavior over the height corresponding to the location of laser sensors and acceleration sensors shown in Figure 1.2. These nodes are from the models with Case 2 Spring mass boundary condition.

Figure 6.3a presents the nodes of interest corresponding to the acceleration sensor locations at the inner leaf and outer leaf. For the inner leaf, Nodes 141, 78 and 14 correspond to the acceleration sensors a3, a5, and a7. The relative base displacement for the inner leaf nodes are compared to the experimental shaking table test results and presented in Figure 6.4. The minima of the time histories are highlighted using a triangle for numerical results and a circle for experimental results.

Similarly, for the outer leaf, Nodes 948, 1012, and 1076 correspond to acceleration sensors a2, a4, and a6 respectively. The relative to base

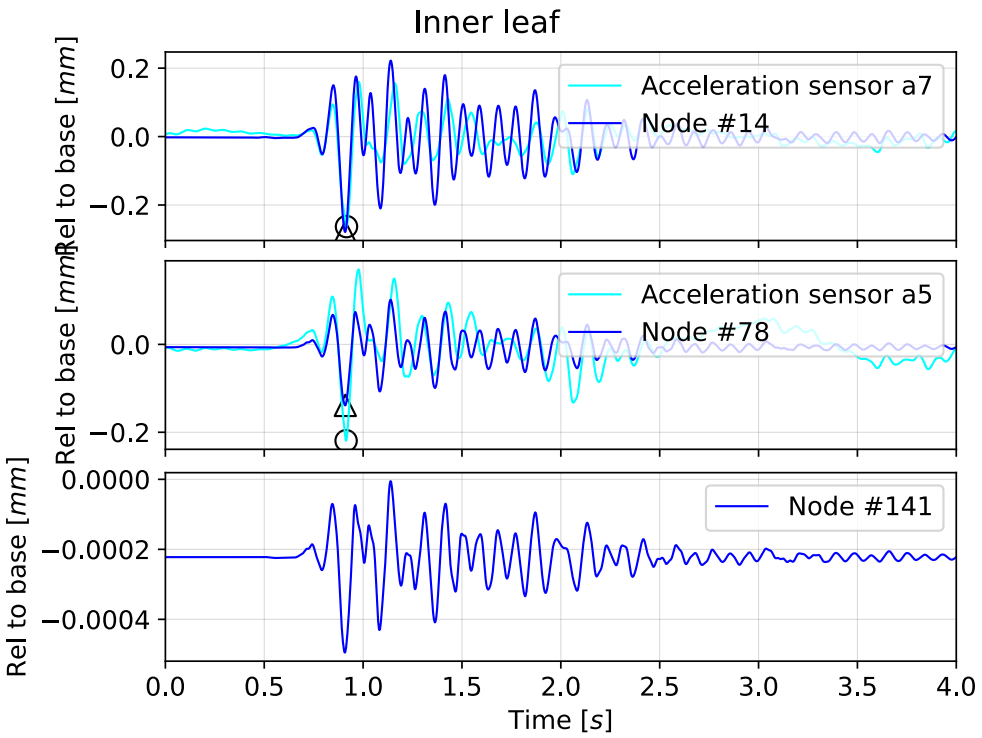

Figure 6.4: Evaluation of minima of relative to base displacement for the nodes corresponding to their respective acceleration sensors of inner leaf for Model 1.

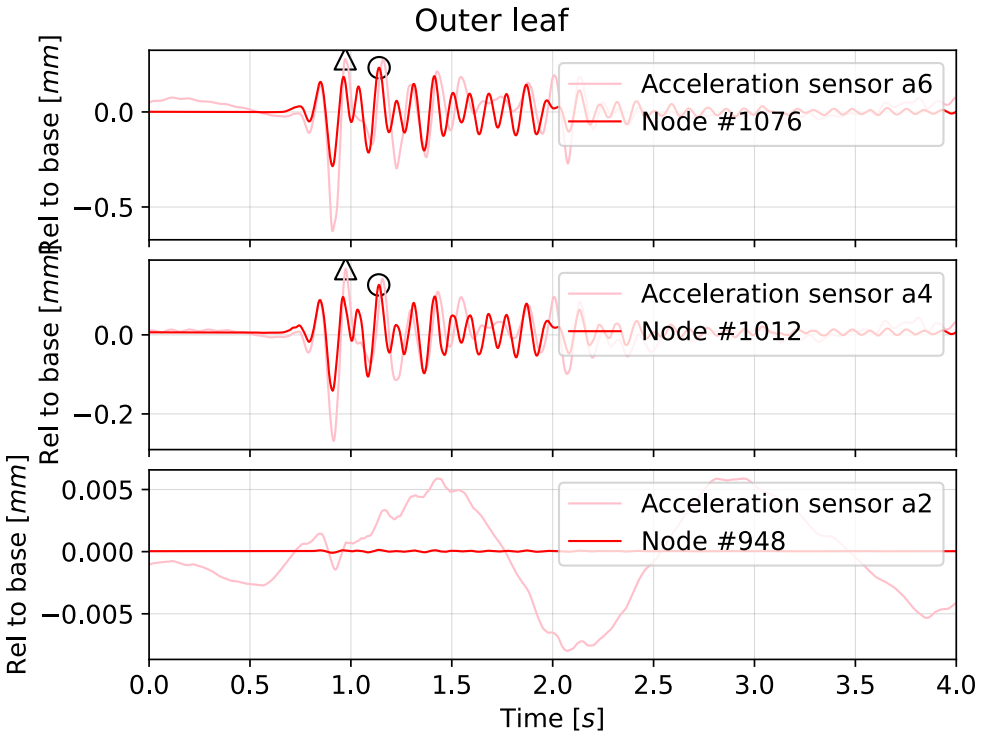

Figure 6.5: Evaluation of maxima of relative to base displacement for the nodes corresponding to their respective acceleration sensors of outer leaf for Model 1.

results for the numerical model and experimental test are shown in Figure 6.5. The maxima of the time histories are highlighted using a triangle for numerical results and a circle for experimental results. These results correspond to Model 1 and its corresponding shaking table test with input signal FHUIZ-DS0-0002.

6.5 LIGHT DAMAGE INITIATION AND DEVELOPMENT

The crack initiation and propagation along the outer leaf during the experimental shaking table tests were monitored using Digital Image Correlation (DIC) technique. The outer leaf was monitored over 6 positions along the height. These locations are specified in Figure 1.2.

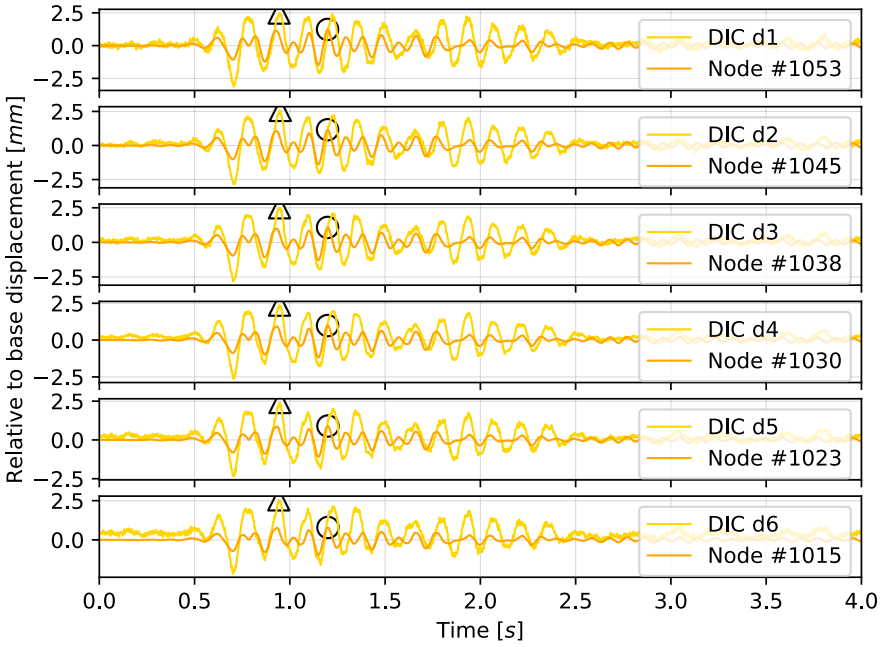

Figure 6.6: Maximas highlighted for the relative to base time history of the nodes corresponding to the laser sensors used for DIC.

Figure 6.3b presented the node of interest along the outer leaf of the finite element models corresponding to the laser sensors using DIC. The relative base displacements of the nodes corresponding to laser sensors are evaluated. Figure 6.6 presents a comparison of numerical and experimental results. The numerical results are evaluated from Model 7 corresponding to the test with input signal **FHUIZ-DS0-0020** (scaling factor = 175%). During the experimental shaking table tests, cracking was observed along the mid-height of the outer leaf.

7 RESULTS AND DISCUSSIONS

In this chapter, the results obtained from the analysis of the finite element models shown in Chapter 5 are presented and discussed. The analysis methods used to evaluate the results of the finite element models were presented in Chapter 6. The results are calibrated on the basis of material properties. The results obtained using ***Initial values*** are presented followed by ***Calibration 1: Reduced steel tie stiffness*** and ***Calibration 2: NPR 998:2020 recommended values***.

7.1 DYNAMIC BEHAVIOR AT MID-HEIGHT: LINEAR ELASTIC PROPERTIES

For such complex models, it is suggested to first evaluate the results using the linear elastic material model. The results are evaluated using the method of analysis presented in Section 6.2.

7.1.1 Initial values

The material properties used to evaluate these results were presented in Table 5.4. These properties were presented in Chapter 3.

The dynamic behavior at the mid-height of the finite element model is compared to the behavior of the test specimen under shaking table tests. The results of two cases of top boundary conditions are presented and compared with the *Linear Phase* results of the shaking table tests.

Figure 7.1 presents results obtained for Models 1 to 6 which belong to the *Linear Phase*. Figure 7.3a presents the dynamic behavior of the models with roller support as the top boundary condition and Figure 7.3b presents the same for models with spring mass as the top boundary condition. The dynamic behavior at mid-height for models with Case 2 top boundary condition was less stiff than models with Case 1 top boundary condition.

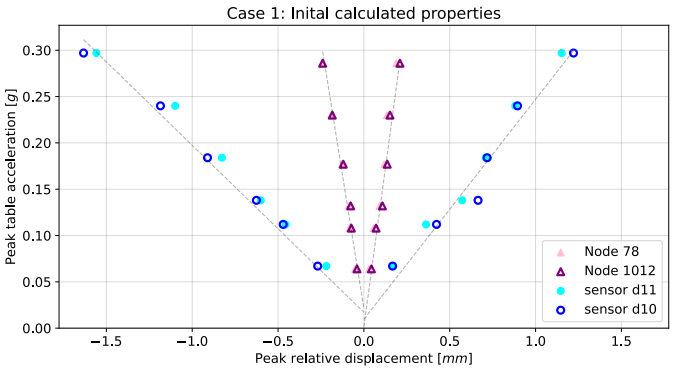

(a) Case 1: Roller support

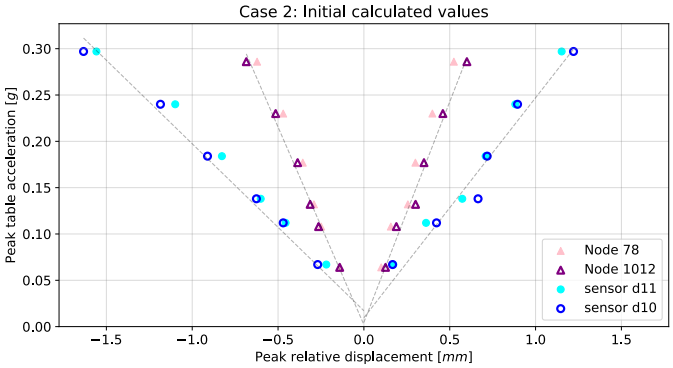

(b) Case 2: Spring-mass support

Figure 7.1: Dynamic behavior of specimen at mid-height evaluated for ***Initial values*** of linear elastic properties. The results are shown for *Nodes 78* and *Node 1012* for the FEM of two cases of top boundary condition.

7.1.2 Calibration 1: Reduction of steel tie stiffness

The results for the finite element model with initially calculated material properties presented the stiff behavior of the finite element model. The first calibration to reduce the stiff behavior of the model was to reduce the stiffness of the steel ties. Figure 7.2 presents the results obtained for finite element models for both cases of top boundary condition.

Material properties	Notation	Inner leaf	Outer leaf	Steel ties	Unit
Young's modulus	E	9658.3	8050	105000	N/mm^2
Poisson's ratio	μ	0.22	0.17	0.3	-
Mass density	ρ	1890	1587	8000	kg/mm^3

Table 7.1: Calibrated linear elastic material properties for ***Calibration 1: Reduced steel tie stiffness***.

Chapter 5 presented that beam elements were used to model the steel tie connections between the inner leaf and outer leaf of the model.

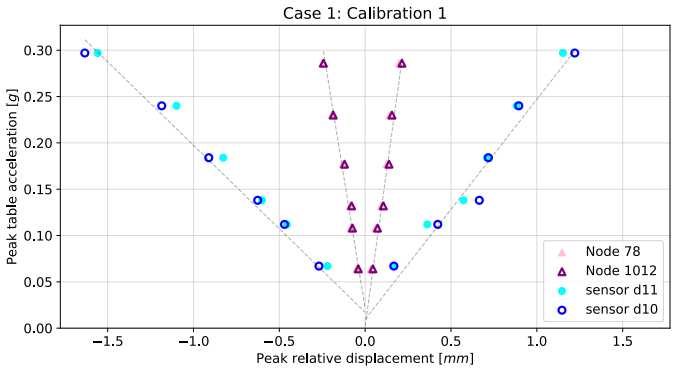

(a) Case 1: Roller support condition

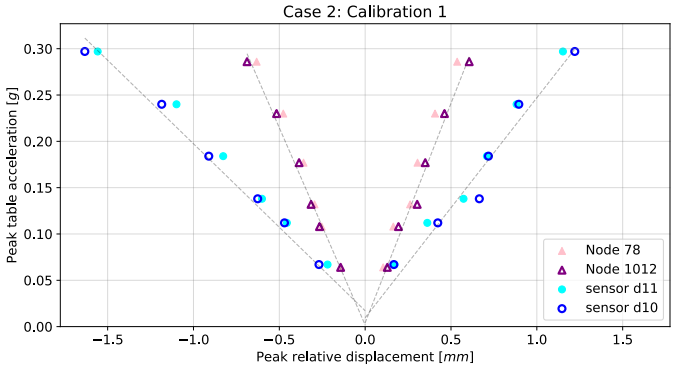

(b) Case 2: Spring-mass support condition

Figure 7.2: Dynamic behavior of specimen at mid-height evaluated for***Calibration 1: Reduced steel tie stiffness*** . The results are shown for *Nodes 78* and *Node 1012* for the FEM of two cases of top boundary condition.

Material properties	Notation	Inner leaf	Outer leaf	Steel ties	Unit
Young's modulus	E	4000	6000	210000	N/mm^2
Poisson's ratio	μ	0.22	0.17	0.3	-
Mass density	ρ	1890	1587	8000	kg/mm^3

Table 7.2: Calibrated linear elastic material properties for ***Calibration 2: NPR 998:2020 recommended values***.

The stiffness of the steel ties is halved to calibrate the dynamic behavior of the numerical models The updated properties are presented in Table 7.1. The reduction of steel tie stiffness did not affect the dynamic behavior at the mid-height significantly.

7.1.3 Calibration 2: NPR 998:2020 recommended values

The second calibration was to use recommended values by NPR998:2020 for the material properties of the inner leaf and the outer leaf.

The calibrated values of material properties are presented in Table 7.2 and its results in Figure 7.3. The stiffness for the steel ties

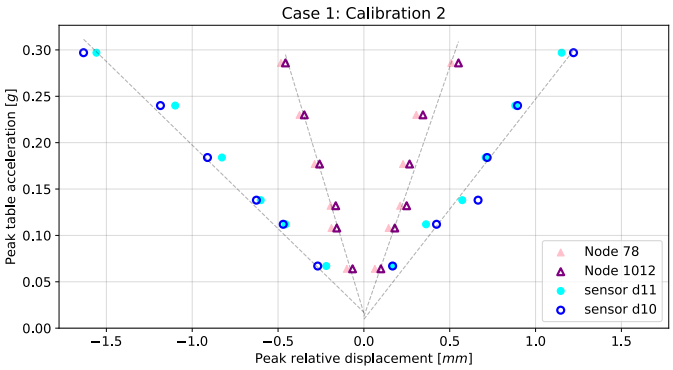

(a) Case 1: Roller support condition

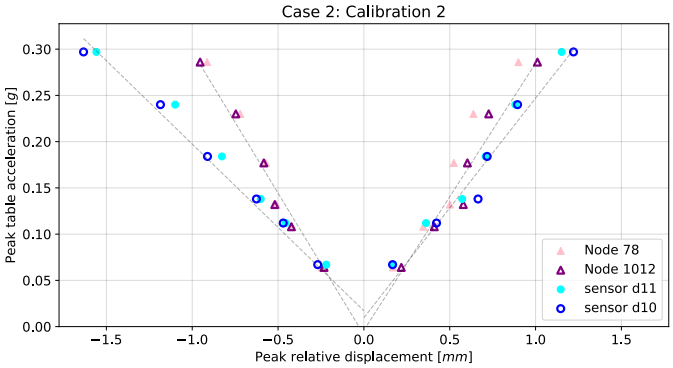

(b) Case 2: Spring-mass support condition

Figure 7.3: Dynamic behavior of specimen at mid-height evaluated for the second calibration by using values recommended by NPR998:2020. The results are shown for Nodes 78 and 1012 for the FEM of two cases of top boundary condition.

was taken as the average value as it has no effect on the dynamic behavior of the model. The second calibration substantially reduced the stiffness of the models with both cases of top boundary condition, especially Case 2 (Spring mass support). For the results of Case 2, the inner leaf still presents to be stiff whereas the behavior of the outer leaf is quite similar to that of the experimental shaking table tests.

7.2 DYNAMIC BEHAVIOR AT MID-HEIGHT: EMM PROPERTIES

The results are evaluated using the method of analysis presented in Section 6.3.

7.2.1 Initial values

Figure 7.4, presents the dynamic behavior at mid-height of the specimen for all the thirteen models. The material properties used were described in Table 5.8 in Chapter 5.

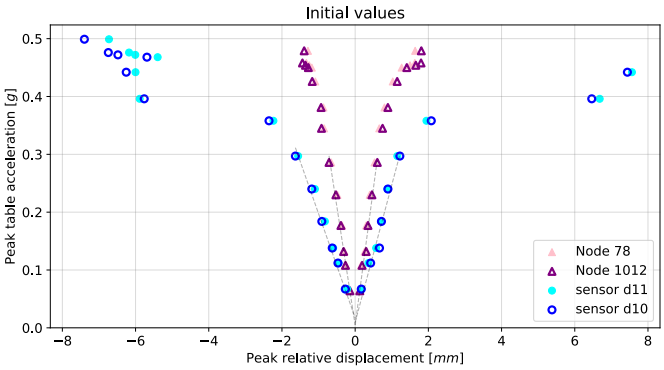

Figure 7.4: Dynamic behavior at mid-height for ***Inital values*** using EMM as a material model.

A linear trend can be observed for the models with PTA of up to 0.4 g. This was expected as the *Linear Phase*, Models 1 to 6 with PTA of upto 0.3 g showed stiff behavior for the linear elastic material model. The peak relative displacement does not go beyond 2 mm for the finite element models, whereas the experimental shaking table test results exceeded that limit for PTA more than 0.3 g.

7.2.2 Calibration 1: Reduction of steel tie stiffness

Similar to the calibration of results with linear elastic material mode, the first calibration chosen was to reduce the stiffness of the steel ties. The stiffness of the steel ties is halved. Figure 7.5 presents the dynamic behavior at the mid-height for FEM and experimental results. This calibration had no effect on the results.

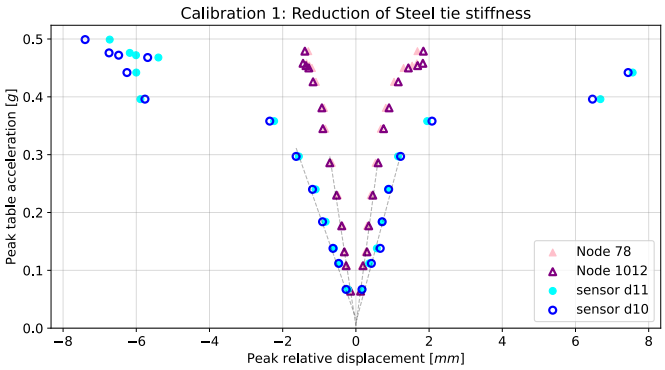

Figure 7.5: Dynamic behavior at mid-height for ***Calibration 1*** using EMM as a material model.

7.2.3 Calibration 2: NPR 998:2020 recommended values

The second calibration of the results was based on the material properties recommended by NPR 998:2020. The calibrated material properties are shown in Table 7.2. The peak relative displacement matches the experimental shaking table tests quite close up to PTA 0.3 g. This behavior was similar to what was observed in the linear elastic material model.

There was a change in the material model did affect significantly the peak relative displacement for PTA above 0.3g. The maximum relative displacement did exceed 2 mm, however, it was only by 0.5 mm.

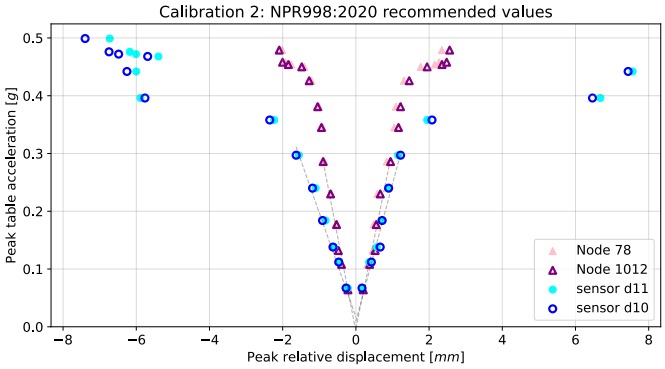

Figure 7.6: Dynamic behavior at mid-height for ***Calibration 2*** using EMM as a material model.

Paramters	Notation	Inner leaf	Outer leaf	Unit
Elastic parameters				
Modulus of Elasticity	E_x	4000	6000	N/mm^2
Modulus of Elasticity	E_y	4000	6000	N/mm^2
Shear modulus	G_xy	1650	2500	N/mm^2
Mass Density	ρ			kg/m^3
Maximum crack width along the thickness Parameter				
Bed joint tensile strength	$f_{ma;x;1;m}$	0.15	0.3	N/mm^2
Fracture energy in tension	Gf_t	0.01	0.01	N/mm
Crushing paramters				
Compressive strength	$f_{ma;m}$	7	10	N/mm^2
Fracture energy in compression	Gf_c	15	15	N/mm
Factor to strain at compressive strength		4	4	
Unloading		secant	secant	
Shear failure parameters				
Bed joint shear friction coefficient	$\nu_{ma;m}$	0.6	0.75	
Friction angle		0.5401	0.6432	
Cohesion		0.225	0.45	N/mm^2
Fracture energy in shear	Gf_v	0.1	0.2	N/mm

Table 7.3: Updated parameters for EMM for ***Calibration 2***.

7.3 DYNAMIC BEHAVIOR OVER THE HEIGHT: EMM PROPERTIES FOR ALL THE TESTS

The results presented in the previous sections availed an insight into the dynamic behavior of the FEM at the mid-height. In this section, the dynamic behavior over the height of the FEM is compared to the experimental shaking table tests. The results presented in this section are evaluated using the Engineering Masonry material model. The results are evaluated using the method of analysis presented in Section 7.2. The minimum relative to base displacement for the inner leaf is compared for Models 1, 7, 9, and 13 and their corresponding shaking table tests. For the outer leaf, the maximum relative to base displacement is plotted corresponding to the locations of the acceleration sensor and laser sensors used for DIC.

7.3.1 Initial values

The dynamic behavior over the height for the ***Initial values*** is presented in Figure 7.7. The results are evaluated using Engineering masonry model properties as same as described in Section 7.2.1.

The translation of the top of the inner leaf is close to the experimental tests. This was due to the spring-mass top boundary condition.

The dynamic behavior after Model 7 showed that the model is not able to deform sufficiently at the mid-height. Linear behavior is observed over the height of the specimen, whereas in the evolution of the experimental tests, it can be observed that there is cracking along the mid-height of the specimen.

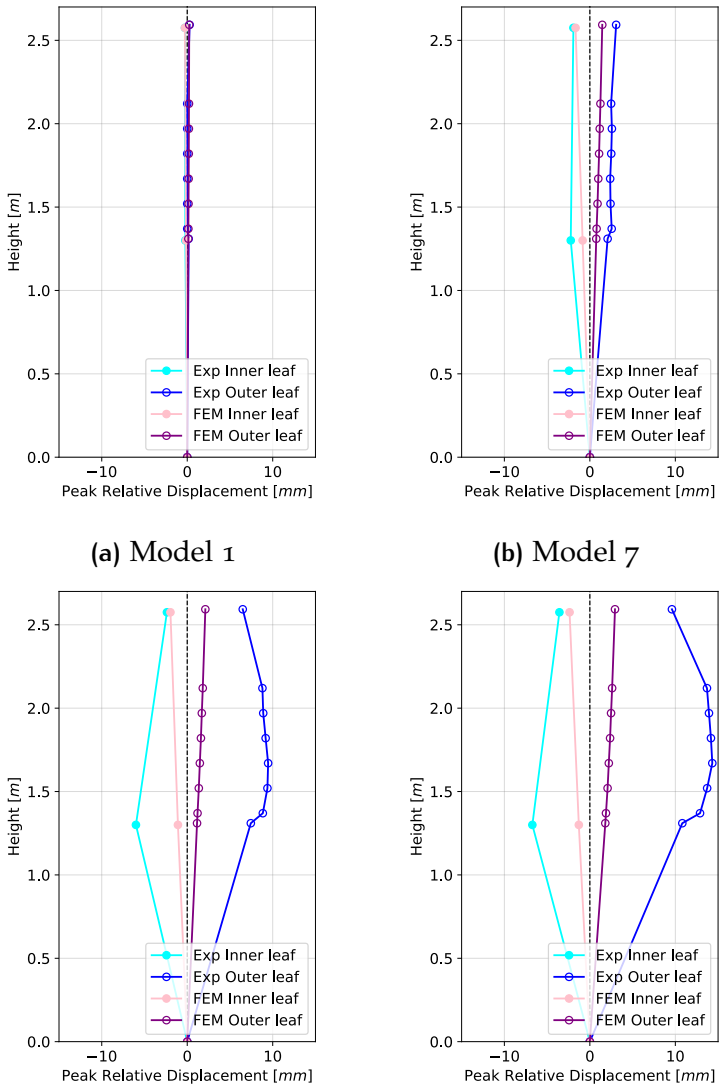

(a) Model 1

(b) Model 7

(c) Model 9

(d) Model 13

Figure 7.7: Evolution of displacement over the height of the models for ***Initial values*** using Engineering Masonry model.

7.3.2 Calibration 1: Reduction of steel tie stiffness

Similar to previous results calibration, the stiffness of the steel ties was halved. Figure 7.8 presents the displacement over height evolution through the model tests. The reduction of the steel tie stiffness did not affect the overall behavior. This was expected based on the observations from previous results.

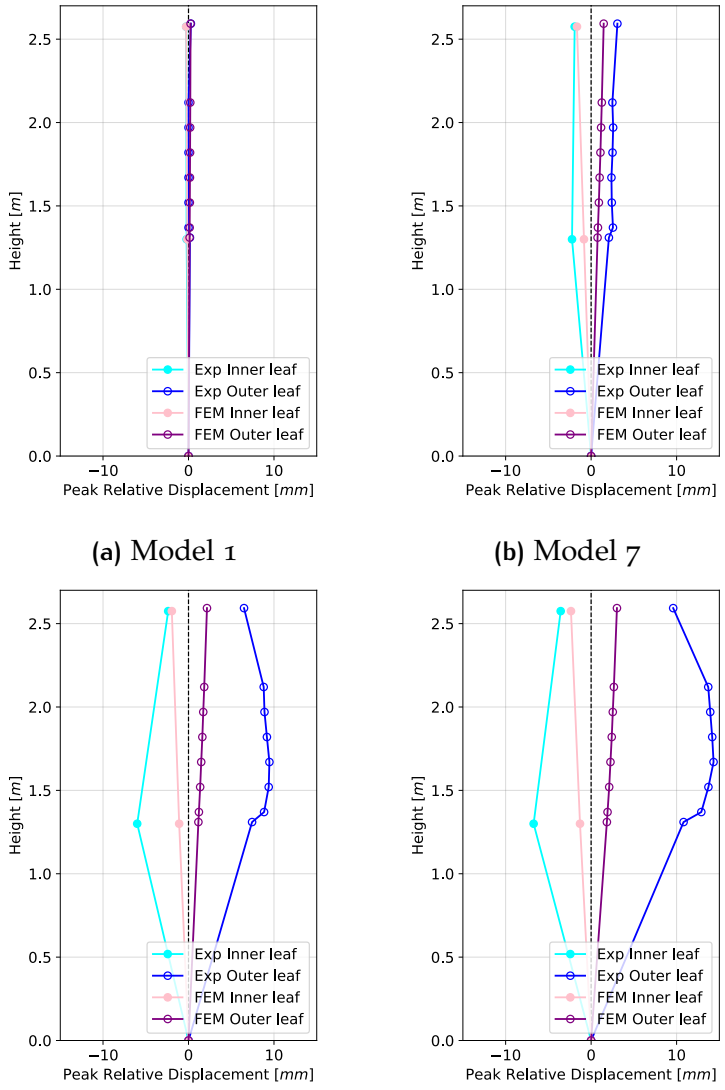

(a) Model 1 (b) Model 7

(c) Model 9 (d) Model 13

Figure 7.8: Evolution of displacement over the height of the models for ***Calibration 1*** using Engineering Masonry model

7.3.3 Calibration 2: NPR 998:2020 recommended values

The material properties were calibrated based on the recommended values from NPR 998:2020. Figure 7.9 presents the displacement over height evolution of the models through the tests. The results presented here correspond to the calibrated material properties recommended by NPR 998:2020. Similar to previous calibrations, the model is not able to deform along the mid-height of the outer leaf or the inner leaf.

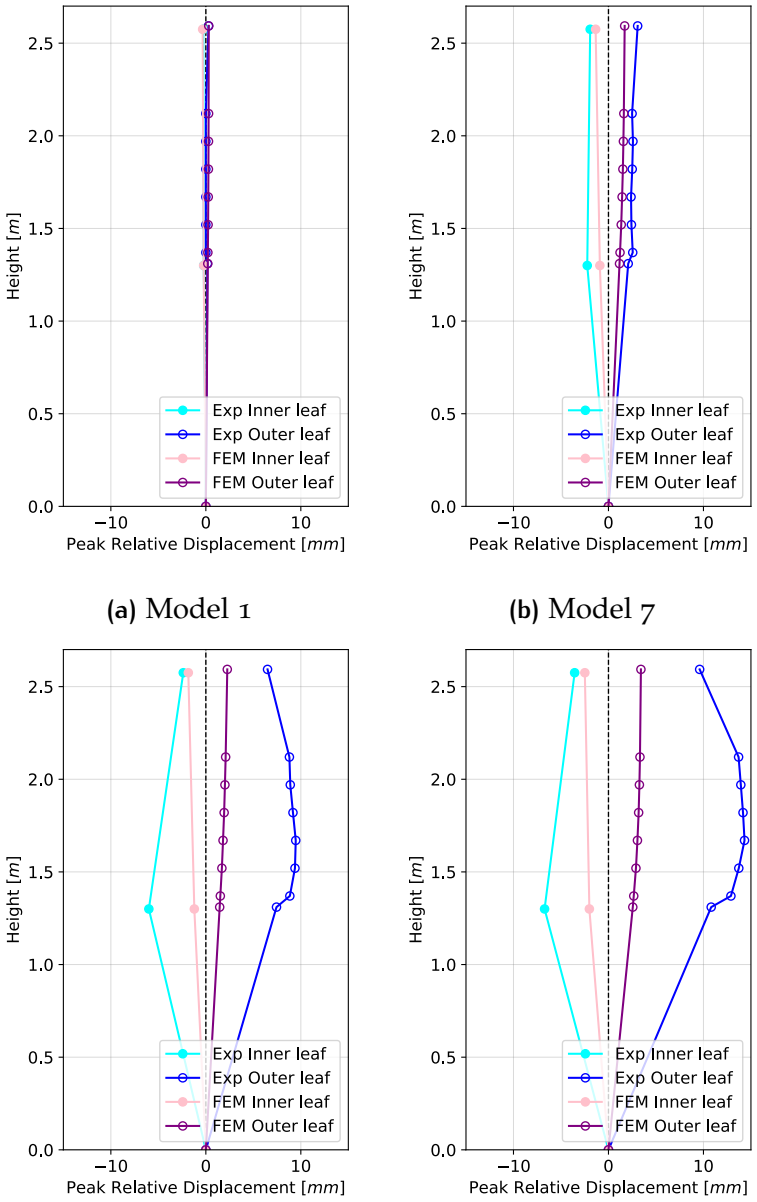

(a) Model 1

(b) Model 7

(c) Model 9

(d) Model 13

Figure 7.9: Evolution of displacement over the height of the models for ***Calibration 2*** using Engineering Masonry model

7.4 LIGHT DAMAGE INITIATION AND PROPAGATION

In this section, the crack pattern development for the three calibrations discussed is presented and discussed. The locations of observations for these crack patterns are above the mid-height of the cavity wall. The results are evaluated using the method of analysis presented in Section 6.5. To have an insight view of the nonlinear behavior in the seismic response, crack pattern figures are presented, which are indicated by the state parameter NCRACK=1 (red color).

7.4.1 Initial values

The crack development is presented in Figure 7.10. Damage was initiated at the support condition of the outer leaf for an input signal of PTA 0.1 g (Model 2). The crack starts propagating over the height on the outside and inside of the outer leaf. At the input signal of PTA 0.24 g (Model 5), a crack initiates at the support condition of the inner leaf as well.

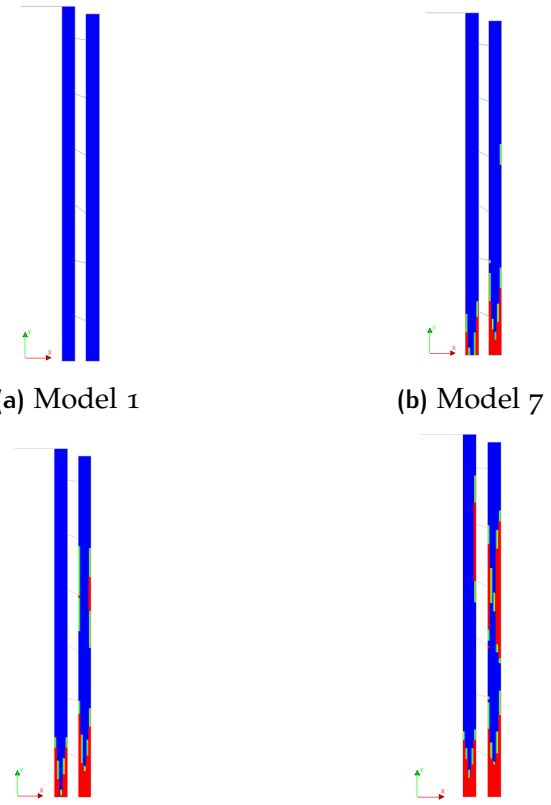

(a) Model 1 **(b)** Model 7

(c) Model 9 **(d)** Model 13

Figure 7.10: Crack patterns at end of the seismic signal for models with ***Initial values*** material properties. Crack is indicated by red color when parameter NCRACK = 1.

During input signalS with PTA 0.36 g (Model 7) and PTA 0.44 g (Model 9), a crack is formed at the outer leaf over the height 1.4 m to 1.6 m. From models with input signal with PTA 0.46 g (Model 8) to 0.49 g (Model 13), cracks are formed along the nodes of steel tie connections between the cavity wall. The crack has propagated through the thickness up to (30 mm)of the outer leaf. On the other hand, the crack along the bottom boundary condition has propagated completely through the thickness of the inner leaf and the outer leaf.

7.4.2 Calibration 1: Reduction of steel tie stiffness

Similar observations for Calibration 1, presented in Figure 7.11. On reduction of stiffness of the steel ties, Crack initiation was observed along the outer leaf for models with an input signal of PTA 0.472 g (Model 11) to PTA 0.5 g (Model 13).

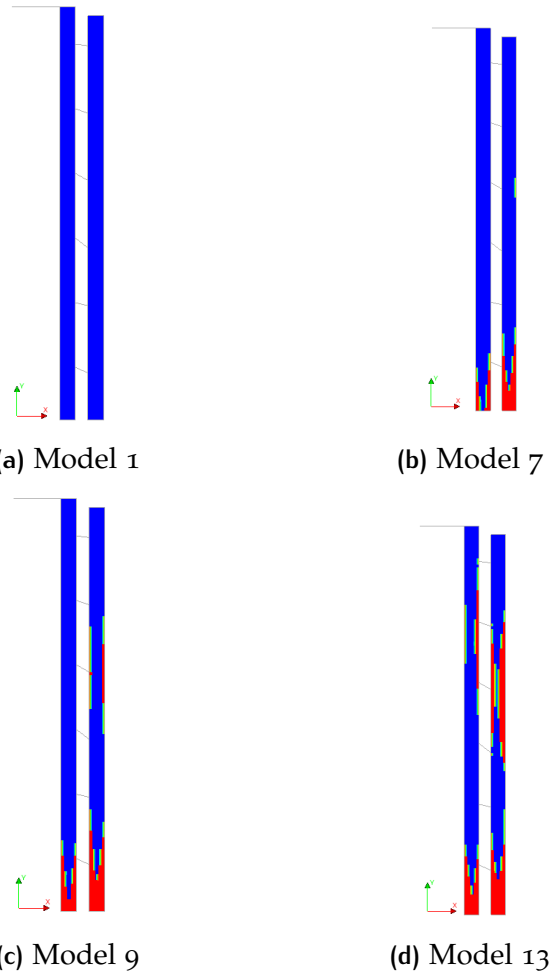

(a) Model 1 (b) Model 7

(c) Model 9 (d) Model 13

Figure 7.11: Crack patterns at end of the seismic signal for models with calibration 1 material properties. Crack is indicated by red color when parameter NCRACK = 1.

Crack initiation and propagation through the outer leaf above the mid-height was an effect of the calibration

7.4.3 Calibration 2: NPR 998:2020 recommended values

The damage development is presented in Figure 7.12. Crack initiation at the bottom support condition of the inner leaf for an input signal of PTA 0.24 g (Model 5) which is at a higher input level than that of the ***Initial values*** results. For the input signal with PTA 0.44 g (Model 9), a crack is formed at the outer leaf over the height 1.4 m to 1.6 m and the inner leaf. Cracks were observed from Model 9 at the steel tie connections.

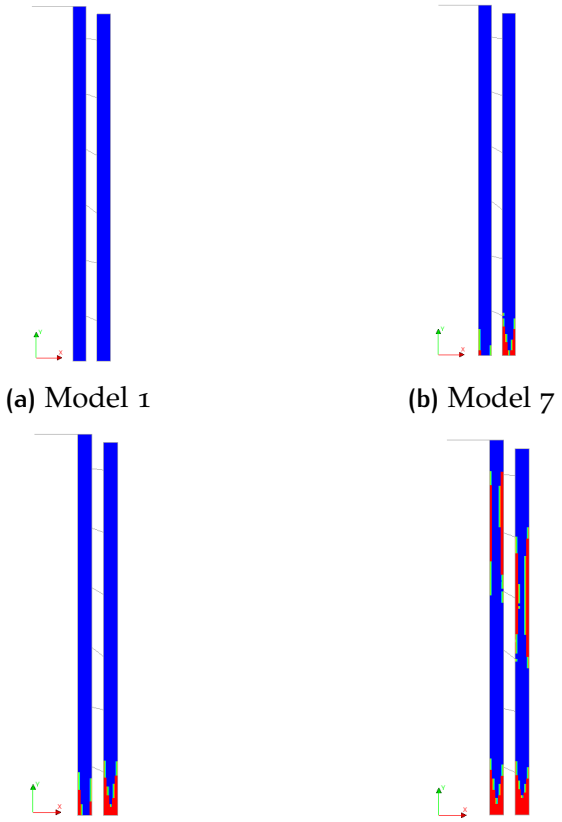

(a) Model 1 (b) Model 7

(c) Model 9 (d) Model 13

Figure 7.12: Crack patterns at end of the seismic signal for models with calibration 2 material properties. Crack is indicated by red color when parameter NCRACK = 1.

8 CONCLUSIONS AND RECOMMENDATIONS

8.1 CONCLUSIONS

TNO conducted out-of-plane shaking table tests on a URM cavity wall to investigate the light damage initiation and propagation. In this research, non-linear time history analysis was conducted on a URM cavity wall to numerically assess the light damage initiation and development of the experimental shaking table tests. The results of the transient analysis conducted on the finite element models were presented and calibrated. The steps taken to answer the main research question are shown in Figure 8.1.

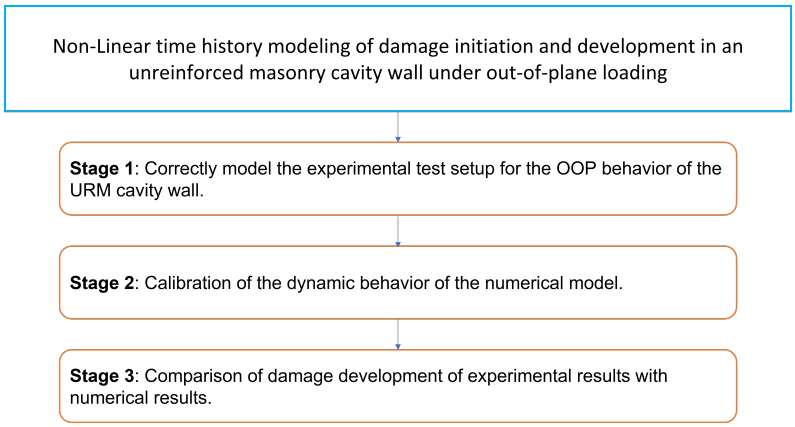

Figure 8.1: Flowchart highlighting the steps to answer the main research question of this study.

In order to perform the transient analysis, finite element models were set up. The finite element models were set up on the basis of the thirteen input signals used for the shaking table tests, thereby creating thirteen models. Based on the results obtained from the experimental shaking table tests, the models were classified into two phases, the Linear phase (Models 1 to 6) and the Nonlinear phase (Model 7 to 13).

The models were initially analyzed using Eigenvalue analysis in order to check the dynamic properties. Due to the complexity of the models, the Linear phase (Models 1 to 6) was first evaluated using the Linear elastic material model. Followed by conducting a transient analysis of all the models of both the Linear phase and Non-linear phase with the Engineering Masonry Model as the material model.

The results were compared to the experimental shaking table test results. Conclusions are drawn on the basis of the analyses conducted and the results compared are as follows:

Input seismic signal

- Baseline drift was observed on the application of raw measured acceleration data as an input acceleration control to the models.
- The baseline drift phenomenon is reduced by removing the low-frequency content up to 5 Hz of the input acceleration signal.
- Truncation of input acceleration signal significantly increases the baseline drift effect and the filter settings need to be adjusted accordingly.

Calibration of model

- The eigenvalue analysis showed that the model can be calibrated either on the basis of boundary conditions or material properties.
- The first eigenfrequency is significantly affected by the choice of top boundary condition. The second eigenfrequency is affected by the material properties, especially the stiffness of the inner leaf and the outer leaf.
- The preliminary eigenvalue analysis showed that for Case 1: Roller support as a top boundary condition, the dynamic properties of the model were substantially higher than that of the experimental setup.
- For Case 2: Spring mass support at the top boundary condition, the spring connection to the top of the inner leaf was calibrated to match the first natural frequency of the experimental setup.
- The eigenvalue analysis of models with ***Initial values*** of material properties, matched the eigenvalues of the test specimen but the dynamic behavior was stiffer.
- The first step to calibrate the results was to reduce the steel tie stiffness. The steel tie stiffness was halved (***Calibration 1; Reduction of steel tie stiffness***). The dynamic behavior was not affected by this calibration.
- The second calibration was to use the values recommended by NPR998:2020 (***Calibration 2: NPR 998:2020 recommended values***). The dynamic behavior at the mid-height for the Linear

phase models closely followed that of the shaking table test results. However, the Non-linear phase models could not predict failure which was observed during the shaking table tests.

Light damage initiation and development

- The transient analysis of the models did not predict the extent of damage correctly with respect to the shaking table test results. The peak crack width during the transient analysis could not exceed 0.1 *mm* (Crack width corresponding to Damage state 1).
- The models did however present the damage propagation over the height of the URM cavity wall. The damage propagation was evaluated by checking the integration points where the bed-joint tensile strength was exceeded.
- For ***Initial values*** of material properties, the damage was initiated at the bottom boundary condition of the outer leaf for input seismic signal with peak table acceleration of 0.078 g. At the input signal with peak table acceleration (PTA) of 0.2 g, the damage was initialized at the bottom boundary condition of the inner leaf. For input seismic signals above peak table acceleration (PTA) of 0.23 g, the damage initiated and propagated around the mid-height of the outer leaf.
- Unlike shaking table tests, the damage localization was not observed in the models. The damage was smeared over the mid-height of the outer leaf and the bottom boundary condition.
- For ***Calibration 1: Reduced steel tie stiffness*** values, damage development followed the same path which was observed for previous values of material properties. In addition to this, the damage was also initiated around the steel tie connections above the mid-height of the outer leaf for the input signal with peak table acceleration (PTA) of 0.2 g.
- For ***Calibration 2: NPR 998:2020 recommended values*** values, damage development followed the same path which was observed for ***Initial values*** of material properties. However, the damage initialized for the input signal with a higher peak table acceleration of 0.23 g instead of 0.078 g.
- For all the calibrations of material properties, the damage initialized and propagated through the thickness of the outer leaf followed by the inner leaf at the bottom boundary condition. It can be concluded from this that a rocking crack was formed at the bottom of the outer leaf. The rocking crack could have been initialized for the input signal with a peak table acceleration of 0.1 g.

8.2 RECOMMENDATIONS

Further research is needed for reliable assessment of light damage initiation and development for URM cavity walls under out-of-plane loading. On the basis of the results and conclusions presented, the following recommendations are suggested to further the research:

Analytical model

- For accurate calibration of the numerical model, it is recommended to analytically analyze the experimental setup. The analytical model presented in this study can serve as a starting point.

Boundary condition

- The boundary conditions need further research. The bottom boundary condition specifically. The formation of a rocking crack at the bottom of the cavity wall can be modeled as hinge support.
- Another way to model this is by creating multiple models with different bottom boundary conditions on the basis of material properties and peak table acceleration levels of the input signal. For input signal with PTA lower than 0.07 g the fixed boundary condition, for PTA levels between 0.07 g, hinge support is recommended.

Light damage initiation and development

- The assessments might be carried out taking into account the accumulated damage to the structure by applying a series of sequentially incrementally scaled seismic signals to the model.
- Variation of material parameters, particularly the bed joining tensile strength f_t and fracture energy Gf_t. These parameters can be optimized by using the optimization algorithm suggested in [19]. The crack widths obtained by the DIC technique in the experimental tests can serve as a valid check for calibration of tensile strength and fracture energy in tension.
- To obtain damage localization similar to the shaking table tests, a micro-modeling approach is suggested. Modeling the brick and mortar as separate units would localize the damage initialization and development at the mortar for such low-intensity input seismic signals.

BIBLIOGRAPHY

[1] EN 1996-1-1: Eurocode 6: Design of masonry structures - Part 1-1: General rules for reinforced and unreinforced masonry structures.

[2] Bathe, K., Structural, E. W. E. E. ., and 1972, u. Stability and accuracy analysis of direct integration methods. *Wiley Online Library 1*, 3 (1973), 283–291.

[3] Bronkhorst, A. J., and Geurts, C. P. Out-of-plane shaking table tests on Dutch building products. *Proceedings of the International Conference on Structural Dynamic , EURODYN 2*, January 2021 (2020), 3228–3244.

[4] Dam, J. v. Validation of efficient numerical models for out-of-plane bending of unreinforced masonry walls. 170.

[5] Dizhur, D., and Ingham, J. M. Seismic Improvement of Load-bearing Unreinforced Masonry Cavity Walls.

[6] Dokainish, M. A., and Subbaraj, K. A survey of direct time-integration methods in computational structural dynamics—I. Explicit methods. *Computers & Structures 32*, 6 (1 1989), 1371–1386.

[7] D'Altri, A. M., Sarhosis, V., Milani, G., Rots, J., Cattari, S., Lagomarsino, S., Sacco, E., Tralli, A., Castellazzi, G., and de Miranda, S. *Modeling Strategies for the Computational Analysis of Unreinforced Masonry Structures: Review and Classification*, vol. 27. Springer Netherlands, 2020.

[8] Fea Bv, D. DIANA FEA BV and TU Delft DIANA FEA report 2016-DIANA-R1601 TU Delft Structural Mechanics CiTG report CM-2016-17 DIANA Validation report for Masonry modelling Date Validation masonry models under seismic conditions. Tech. rep., 2017.

[9] Felippa, C. A. PROCEDURES FOR COMPUTER ANALYSIS OF LARGE NONLINEAR STRUCTURAL SYSTEMS. *Large Engineering Systems* (1 1977), 60–101.

[10] Giaretton, M., Dizhur, D., da Porto, F., and Ingham, J. M. Construction Details and Observed Earthquake Performance of Unreinforced Clay Brick Masonry Cavity-walls. *Structures 6* (5 2016), 159–169.

[11] Graziotti, F., Tomassetti, U., Kallioras, S., Penna, A., and Magenes, G. Shaking table test on a full scale URM cavity wall building. *Bulletin of Earthquake Engineering 15*, 12 (12 2017), 5329–5364.

[12] Grünthal, G., and Schwarz, J. European Macroseismic Scale 1998 EMS-98 Editor.

[13] Korswagen, P. A., Jonkman, S. N., and Terwel, K. C. Probabilistic assessment of structural damage from coupled multi-hazards. *Structural Safety 76* (1 2019), 135–148.

[14] Korswagen, P. A., Longo, M., and Rots, J. G. High-resolution monitoring of the initial development of cracks in experimental masonry shear walls and their reproduction in finite element models. *Engineering Structures 211* (5 2020), 110365.

[15] Lagomarsino, S., Penna, A., Galasco, A., and Cattari, S. TREMURI program: An equivalent frame model for the nonlinear seismic analysis of masonry buildings. *Engineering Structures 56* (11 2013), 1787–1799.

[16] Lourenço, P. B. *Computational strategies for masonry structures*, vol. 70. 1996.

[17] OKADA, S., and TAKAI, N. Classifications of Structural Types and Damage Patterns of Buildings for Earthquake Field Investigation. *Journal of Structural and Construction Engineering (Transactions of AIJ) 64*, 524 (1999), 65–72.

[18] Pan, C., Zhang, R., Luo, H., and Shen, H. Baseline correction of vibration acceleration signals with inconsistent initial velocity and displacement. *Advances in Mechanical Engineering 8*, 10 (10 2016), 1–11.

[19] Pennings, J. K. Modelling the Out-of-plane Behaviour of Seismically Loaded Unreinforced Masonry Cavity Walls Utilization of Shaking Table Test Data.

[20] Pluijm, R. v. d. *Out-of-Plane Bending of Masonry Behaviour and Strength*. No. 1999. 1999.

[21] Tomassetti, U., Graziotti, F., Penna, A., and Magenes, G. Out-of-plane shaking table tests on URM cavity walls. *Brick and Block Masonry: Trends, Innovations and Challenges - Proceedings of the 16th International Brick and Block Masonry Conference, IBMAC 2016*, June (2016), 1939–1948.

[22] Willis, C. R. Design of unreinforced masonry walls for out-of-plane loading. xi, 333.

[23] Yang, Y.-Z., and Jiang, D.-X. Numerical Integration and Complex Trend Term Elimination of Acceleration Signal in Fault Diagnosis. Tech. rep., 2015.

LIST OF FIGURES

LIST OF TABLES

Table 7.3 Updated parameters for EMM for ***Calibration 2***. 73